

Photometric Biases in Modern Surveys

STEPHEN K. N. PORTILLO,^{1,*} JOSHUA S. SPEAGLE,^{2,*} AND DOUGLAS P. FINKBEINER²

¹*DIRAC Institute, Department of Astronomy
University of Washington
3910 15th Ave NE
Seattle, WA 98195, USA*

²*Harvard-Smithsonian Center for Astrophysics
60 Garden St, MS-10
Cambridge, MA 02138, USA*

ABSTRACT

Most surveys use maximum-likelihood (ML) methods to fit models when extracting photometry from images. We show these ML estimators systematically *overestimate* the flux as a function of the signal-to-noise ratio (SNR) and the number of model parameters involved in the fit. This bias is substantially worse for galaxies: while a 1% bias is expected for a 10σ point source, a 10σ galaxy with a simplified Gaussian profile suffers a 2.5% bias. This bias also behaves differently depending how multiple bands are used in the fit: simultaneously fitting all bands leads the flux bias to become roughly evenly distributed between them, while fixing the position in “non-detection” bands (i.e. forced photometry) gives flux estimates in those bands that are biased *low*, compounding a bias in derived colors. We show that these effects are present in idealized simulations, outputs from the HSC fake object pipeline (SynPipe), and observations from SDSS Stripe 82. Prescriptions to correct for these biases are provided along with more detailed results related to biases in ML error estimation.

Keywords: methods: statistical — methods: data analysis — catalogs — techniques: image processing

1. INTRODUCTION

Astronomers want to know how bright astronomical objects are. Precise flux density measurements are crucial for analyzing time-variable signals when searching for exoplanets, determining precise colors for stellar and galactic modeling, and – in the age of Gaia – deriving accurate bolometric luminosities. For example, the LSST Science Requirements Document¹ states that photometric precision of 1% is needed for weak-lensing studies, supernova cosmology, classifying potentially hazardous asteroids, and to separate out main sequence and giant stars to map the galaxy. Deriving accurate photometry is crucial to maximize the statistical power of downstream analyses.

The process of converting observed photon counts on pixelated images to these measurements are the foundation upon which much of astronomical science is built. Decades ago the gold standard for precision photometry was photoelectric measurement with a photomultiplier tube (e.g. Landolt 1973, 1983). The photons entering an aperture of, e.g., an eight arcsecond radius were detected and counted. In this way, hundreds of stars could be measured with great precision, and these “standard stars” formed the basis of the commonly used photometric systems. Repeat measurements of these standards were impressively consistent, but even the “Landolt Faint Standards” (Landolt 1992) are relatively bright compared to the saturation limit of modern wide-area surveys.

Modern surveys use arrays of pixelated sensors such as charge-coupled devices (CCDs) in the optical/UV bands and mercury-cadmium-telluride (HgCdTe) devices in the near infrared. Surveys then perform “aperture photometry” by adding up all (background-subtracted) counts inside of a circle in an image. This process works well for isolated

Corresponding author: Stephen K. N. Portillo
sportill@uw.edu, jspeagle@cfa.harvard.edu, dfinkbeiner@cfa.harvard.edu

* Equal contribution

¹ <https://docushare.lsstcorp.org/docushare/dsweb/Get/LPM-17>

stars well above the background noise, and forms the basis of, e.g., the Sloan Digital Sky Survey (SDSS) photometric calibration (Padmanabhan et al. 2008).

Aperture photometry, however, has several significant issues that hamper its usage. Since apertures need to be relatively large compared to the seeing of the image to gather the majority of the light from a single source, it cannot be reliably performed in crowded regions where many sources are close together. Shrinking the size of the aperture can resolve this problem but then results in some amount of light from most sources being excluded, necessitating an “aperture correction” that needs to be calibrated. In addition, since all pixels in an aperture generically have equal statistical weight, including those with very little flux from the source, it becomes increasingly difficult to estimate fluxes from faint sources closer to the background. Aperture photometry can also become quite sensitive to issues relating to background estimation: because all counts in the aperture are being added together, these systematic offsets contribute an increasing portion of the counts with increasing aperture size.

In recent years, a more optimal matched filter-based estimator of flux density has generally been used which maximizes the signal-to-noise ratio (SNR) (Turin 1960; Stetson 1987). While this process can be quite complicated for extended sources, for simple point sources the appropriate 2-D “filter” is the point-spread function (PSF). Put another way, PSF photometry involves a parametric generative model of the noiseless data as a function of some parameters θ . Combining this with an appropriate noise model then yields a likelihood function. Maximizing the likelihood then provides an estimate of the flux with the highest SNR.²

Even for point sources, this process is not always straightforward. While aperture photometry simply requires an appropriately-sized aperture, PSF photometry relies on having an accurate model of the underlying source. This requires knowing the PSF precisely across the image to avoid applying a mismatched filter. While for space-based telescopes the PSF can be quite stable, for ground-based surveys it varies as a function of time and position in the focal plane to such a degree that it can cause flux errors of 1 – 2%, dominating the error budget of bright stars (e.g. Padmanabhan et al. 2008).

Furthermore, while PSF photometry can perform better than aperture photometry for fainter objects by avoiding “overweighting” the background, it still struggles in crowded regions where the measured parameters for objects become covariant with those of close neighbors (or even bright neighbors that are not so close). In the extremely crowded limit, the challenge of estimating the PSF and the background level may become severe. These questions are explored elsewhere (Brewer et al. 2013; Portillo et al. 2017) and are not the focus of this paper.

Finally, although PSF photometry (in theory) maximizes the SNR (i.e. is most *precise*), that **does not** mean that it is unbiased (i.e. is most *accurate*) or gives proper errors (i.e. has appropriate *coverage*). While there are many biases/systematic errors that can appear in photometry (cf. Nyland et al. 2017), in this paper we show that PSF photometry and similar maximum-likelihood (ML) techniques *do* give rise to a bias. We show that this leads the estimated flux density estimates to generally be biased high, and that it broadly arises from PSF photometry “over-fitting” the data *in a way that breaks symmetries*. While this bias is generally small (a $\sim 1\%$ effect at 10σ for a point source) and likely not be of concern for an individual source, its impact may be magnified when using a large population of low signal-to-noise sources.

In this work, we present corrections for this bias and consider its implications for point sources, galaxies, and multi-band fitting. We first introduce a simplified version of maximum-likelihood model fitting photometry with a single source and Gaussian noise in Section 2. We derive the bias in the maximum-likelihood flux for a point source and the corresponding uncertainty in correcting it in Section 3. In Section 4, we show how covariances between parameters inflate the errors from the estimates provided in Section 2. We show that the bias is larger for objects with more parameters and derive expressions for a galaxy with a 2-D Gaussian profile in Section 5. In Section 6, we consider multi-band photometry in both the forced photometry and simultaneous fit case and show that this bias remains present, with different behaviors in each case. In Section 7, we show that this bias is present in mock data pipelines and SDSS data. We discuss in 8 and conclude in Section 9.

All the data and code used to create the plots presented in the paper are available online at https://github.com/joshspeagle/phot_bias. We invite readers to (re-)create their own plots and investigate the nature of this bias for themselves.

2. MAXIMUM-LIKELIHOOD PHOTOMETRY

² This procedure does not take any “prior beliefs” into account, which are required to obtain appropriate estimates under a Bayesian statistical framework.

Consider an $n \times m$ footprint of a pixelated image containing only one point source at some true position (x^*, y^*) with some true flux density f^* . Assume the pixel-convolved point spread function (PSF) is constant throughout the footprint and is exactly known. Let the value of the pixel-convolved PSF in pixel i for a point source located at position (x, y) be $p_i(x, y)$. For notational convenience, the values across the whole image will be modeled as the $nm \times 1$ column vector $\mathbf{p}_{x,y} \equiv \mathbf{p}(x, y) = \{\dots, p_i(x, y), \dots\}$.

Assume that an estimate of the sky background³ has been subtracted from the footprint and that (residual) sky background (henceforth just the “sky background”) in the footprint is Normally distributed with $nm \times 1$ mean column vector \mathbf{b}^* and $nm \times nm$ covariance matrix \mathbf{C} , where the noise \mathbf{C} is known but the mean bias \mathbf{b}^* is not. The observed background noise in our pixels $\hat{\mathbf{b}} \equiv \{\hat{b}_1, \dots, \hat{b}_{nm}\}$ is then distributed as

$$\hat{\mathbf{b}} \sim \mathcal{N}(\mathbf{b}^*, \mathbf{C}) \quad (1)$$

where $\mathcal{N}(\boldsymbol{\mu}, \mathbf{C})$ is the multivariate Normal distribution with mean vector $\boldsymbol{\mu}$ and covariance matrix \mathbf{C} .

In the case where the background noise is independently and identically distributed (iid) with mean b^* and variance σ^2 the noise in each pixel follows

$$\hat{b}_i \sim \mathcal{N}(\mu = b^*, \sigma^2 = \sigma^2) \quad (2)$$

and the mean and covariance become $\mathbf{b}^* = \{b^*, \dots, b^*\}$ and $\mathbf{C} = \text{diag}(\{\sigma^2\})$. Although we will often use vector/matrix notation for compactness, we will derive results assuming the iid case throughout the main text. Some corresponding results for the general case are included in Appendix A.

Excluding noise from the sky background, the value of the model image for a point source at location (x, y) and with flux density f is

$$\mathbf{f}(x, y) = f\mathbf{p}_{x,y} \quad (3)$$

The $nm \times 1$ observed flux densities $\hat{\mathbf{f}}$ within the footprint for our object with true flux density f^* at position (x^*, y^*) are then distributed as

$$\hat{\mathbf{f}}(x^*, y^*, \mathbf{b}^*) = \mathbf{f}^*(x^*, y^*) + \hat{\mathbf{b}} \sim \mathcal{N}(f^*\mathbf{p}_{x^*,y^*} + \mathbf{b}^*, \mathbf{C}) \quad (4)$$

The log-likelihood for a model consisting of a single point source at location (x, y) with flux f and background \mathbf{b} is then

$$\ln \mathcal{L}(x, y, f, b) = -\frac{nm}{2} \ln(2\pi\sigma^2) - \frac{1}{2\sigma^2} \sum_i (\hat{f}_i - fp_i(x, y) - b)^2 \quad (5)$$

When extracting photometry, most often a **maximum-likelihood (ML)** approach is used. While ML estimators have been widely studied in the statistics literature, we derive some basic results for their application to photometry in this section for completeness. These results are already known in the literature and appear in, for example, King (1983).

2.1. Flux Density

Denote the maximum-likelihood (i.e. best-fit) flux for a given the position (x, y) and background \mathbf{b} as $f_{\text{ML}}(x, y, \mathbf{b})$. By definition, the partial derivative of the log-likelihood at $f_{\text{ML}}(x, y, \mathbf{b})$ with respect to f is zero such that

$$\partial_f \ln \mathcal{L}(x, y, f_{\text{ML}}, b) = \frac{1}{\sigma^2} \sum_i (\hat{f}_i - b)p_i(x, y) - f_{\text{ML}}p_i^2(x, y) = 0 \quad (6)$$

where $\partial_f \equiv \partial/\partial f$. This yields

$$f_{\text{ML}}(x, y, b) = \frac{\sum_i (\hat{f}_i - b)p_i(x, y)}{\sum_i p_i^2(x, y)} \quad (7)$$

which is equivalent to using the PSF centered at (x, y) as a matched filter against the background-subtracted image.

We can construct a naive estimate of the error/uncertainty in the maximum-likelihood flux density estimate $\tilde{\sigma}_f(x, y)$ by calculating the (negative inverse of) the second derivative with respect to flux density

$$\tilde{\sigma}_f^2(x, y) \equiv -(\partial_f^2 \ln \mathcal{L})^{-1} = \frac{\sigma^2}{\sum_i p_i^2(x, y)} \equiv \boxed{A_{\text{psf}}(x, y) \times \sigma^2} \quad (8)$$

³ We define the sky background to be any flux *not* coming from the sources that are being cataloged, eg. scattered light from the atmosphere and telescope, dark current, and unresolved sources.

where $A_{\text{psf}}(x, y) \equiv 1/\sum_i p_i^2(x, y)$ is the ‘‘effective area’’ of the PSF. This uncertainty is proportional to the background noise σ and effective PSF area $\sqrt{A_{\text{psf}}(x, y)}$ (i.e. is larger when the PSF is broader). The estimate is naive because it ignores the possible covariances between flux density and other parameters, which we address in Section 4.

As an example, a circular Gaussian PSF with a standard deviation of s pixels has an effective area of

$$A_{\text{psf}}^{\text{G}} \rightarrow 4\pi s^2 \quad (9)$$

in the oversampled limit where $(n, m) \gg s \gg 1$ (i.e. the footprint is large compared to the size of the PSF which is also large compared to the size of a single pixel).

2.2. Position

We can define the maximum-likelihood positions $(x_{\text{ML}}, y_{\text{ML}})$ the same way by setting the partial derivative of the log-likelihood with respect to (x, y) to 0. Using x_{ML} as a representative case we get

$$\partial_x \ln \mathcal{L}(x_{\text{ML}}, y, f, b) = \frac{f}{\sigma^2} \sum_i \left((\hat{f}_i - b) - f p_i(x_{\text{ML}}, y) \right) \partial_x p_i(x_{\text{ML}}, y) = 0 \quad (10)$$

Similarly, the naive error/uncertainty in $(x_{\text{ML}}, y_{\text{ML}})$ can be found by calculating the second derivative with respect to position:

$$\tilde{\sigma}_x^2(x_{\text{ML}}, y, f, b) = \frac{\sigma^2}{f^2} \left(\sum_i (\partial_x p_i(x_{\text{ML}}, y))^2 - \frac{1}{f} \left((\hat{f}_i - b) - f p_i(x_{\text{ML}}, y) \right) \partial_x^2 p_i(x_{\text{ML}}, y) \right)^{-1} \quad (11)$$

This expression has two components. The first involves the square of the first derivative of the pixel-convolved PSF $(\partial_x p_i)^2$, while the second involves the second derivative of the pixel-convolved PSF $\partial_x^2 p_i$ weighted by (fractional) model residuals. Assuming that the residuals are sufficiently small relative to f and the PSF varies sufficiently slowly across the footprint, we can ignore this term and approximate the error as

$$\tilde{\sigma}_x^2(x_{\text{ML}}, y, f) \approx \frac{1}{f^2} \frac{\sigma^2}{\sum_i (\partial_x p_i(x_{\text{ML}}, y))^2} \equiv \boxed{S_{\text{psf}}(x_{\text{ML}}, y) \times \left(\frac{f^2}{\sigma^2} \right)^{-1}} \quad (12)$$

where $S_{\text{psf}}(x, y) \equiv 1/\sum_i (\partial_x p_i(x_{\text{ML}}, y))^2$ is the ‘‘effective smoothness’’ of the PSF, analogous to the effective area $A_{\text{psf}}(x, y)$. Note that the position error is directly proportional the effective PSF smoothness $\sqrt{S_{\text{psf}}(x, y)}$ and inversely proportional to the signal-to-noise ratio (SNR) f/σ .

As above, for the case with a circular Gaussian PSF with a standard deviation of s pixels, the effective smoothness is

$$S_{\text{psf}}^{\text{G}} \rightarrow 8\pi s^4 = 2s^2 A_{\text{psf}} \quad (13)$$

in the oversampled limit for $(n, m) \gg s \gg 1$. This gives a corresponding position error of

$$\sigma_x^2 \rightarrow \frac{2s^2 A_{\text{psf}}^{\text{G}} \sigma^2}{f^2} = 2s^2 \left(\frac{f^2}{\tilde{\sigma}_f^2} \right)^{-1} \quad (14)$$

where $\tilde{\sigma}_f^2$ is the naive flux density error estimate from §2.1.

2.3. Background

For a given flux density f and position (x, y) , we can solve for the maximum-likelihood background b_{ML} by again taking the first derivative

$$\partial_b \ln \mathcal{L}(x, y, f, b_{\text{ML}}) = \frac{1}{\sigma^2} \sum_i \hat{f}_i - f p_i(x, y) - b_{\text{ML}} = 0 \quad (15)$$

and setting it to 0. The ML solution is

$$b_{\text{ML}}(x, y, f) = \frac{1}{nm} \sum_i \hat{f}_i - f p_i(x, y) \quad (16)$$

The associated naive errors then are

$$\boxed{\tilde{\sigma}_b^2 = \frac{\sigma^2}{nm} \equiv \frac{\sigma^2}{A}} \quad (17)$$

where $A = nm$ is the area of the footprint.

This result shouldn't be surprising, since it implies that the maximum-likelihood background is just the mean residual between the model $f\mathbf{p}_{x,y}$ and the data $\hat{\mathbf{f}}$ in our given $n \times m$ footprint. Since we have assumed a fixed value b across the footprint, this is summed over all the pixels. Results for the general case where the background is actually a function of a k nuisance parameters $\boldsymbol{\beta}$ across the footprint are outlined in Appendix B.

3. BIAS IN MAXIMUM-LIKELIHOOD ESTIMATES

While ML estimators are *consistent* estimators (i.e. $f_{\text{ML}} \rightarrow f^*$ as $f/\sigma_f \rightarrow \infty$) assuming no model mismatch, they are *not* guaranteed to be unbiased at any finite SNR. In this section, we derive estimates of the expected bias between the ML flux density estimate f_{ML} and the true flux density f^* along with its associated variance in the ideal case where (x^*, y^*, b^*) are known (§3.1) and the general case where it is not (§3.2). A schematic outline of our results is illustrated in Figure 1.

3.1. Ideal Case

It is helpful to rewrite the noisy observed flux densities $\hat{\mathbf{f}}$ in terms of **random variables** such that

$$\hat{f}_i = f^* p_i(x^*, y^*) + b^* + \sigma Z_i \sim \mathcal{N}(f^* p_i(x^*, y^*) + b^*, \sigma^2) \quad (18)$$

where each $Z_i \sim \mathcal{N}(0, 1)$ is an iid random variable drawn from the standard Normal distribution with mean $\mu = 0$ and variance $\sigma^2 = 1$. This represents a re-framing of the underlying data generating process: start with our true underlying model $f^*\mathbf{p}(x^*, y^*) + \mathbf{b}^*$ and add on a particular value comprised of Z_i drawn from $\mathcal{N}(0, 1)$ scaled by the standard deviation σ .

Given equation (18), the likelihood at the true position (x^*, y^*) and background b^* then reduces to

$$\ln \mathcal{L}(x^*, y^*, f, b^*) = -\frac{A}{2} \ln(2\pi\sigma^2) - \frac{1}{2\sigma^2} \sum_i ((f^* - f)p_i(x^*, y^*) + \sigma Z_i)^2 \quad (19)$$

Setting the partial derivative $\partial_f \ln \mathcal{L} = 0$ then allows us to write the ML flux density estimate as

$$f_{\text{ML}}(x^*, y^*, b^*) = f^* + \frac{\sigma}{\sum_i p_i^2(x^*, y^*)} \sum_i Z_i p_i(x^*, y^*) \quad (20)$$

We can rewrite this by noticing that the latter term is actually normally distributed such that

$$\frac{\sigma}{\sum_i p_i^2(x^*, y^*)} \sum_i Z_i p_i(x^*, y^*) \sim \mathcal{N}\left(0, \frac{\sigma^2}{\sum_i p_i^2(x^*, y^*)} = \tilde{\sigma}_f^2(x^*, y^*)\right) \quad (21)$$

where the equality comes from equation (8). This implies that the ML flux density estimate is distributed as

$$\boxed{f_{\text{ML}}(x^*, y^*, b^*) \sim \mathcal{N}(f^*, \sigma_f^2(x^*, y^*))} \quad (22)$$

since the naive error estimate $\tilde{\sigma}_f^2(x^*, y^*)$ is equivalent to the true error $\sigma_f^2(x^*, y^*)$ in the single parameter case (see §4). In other words, given the true values of (x^*, y^*, \mathbf{b}^*) , the ML flux density estimate f_{ML} is an *unbiased* estimate of the true flux density f^* with a variance of $\sigma_f^2(x^*, y^*)$ corresponding to the true variance.

3.2. General Case

Following our random variable notation above, at the true values (x^*, y^*, f^*, b^*) of the position, flux density, and background, respectively, we can rewrite the likelihood of the noisy data as

$$\ln \mathcal{L}(x^*, y^*, f^*, b^*) = -\frac{A}{2} \ln(2\pi\sigma^2) - \frac{1}{2} \sum_i Z_i^2 \quad (23)$$

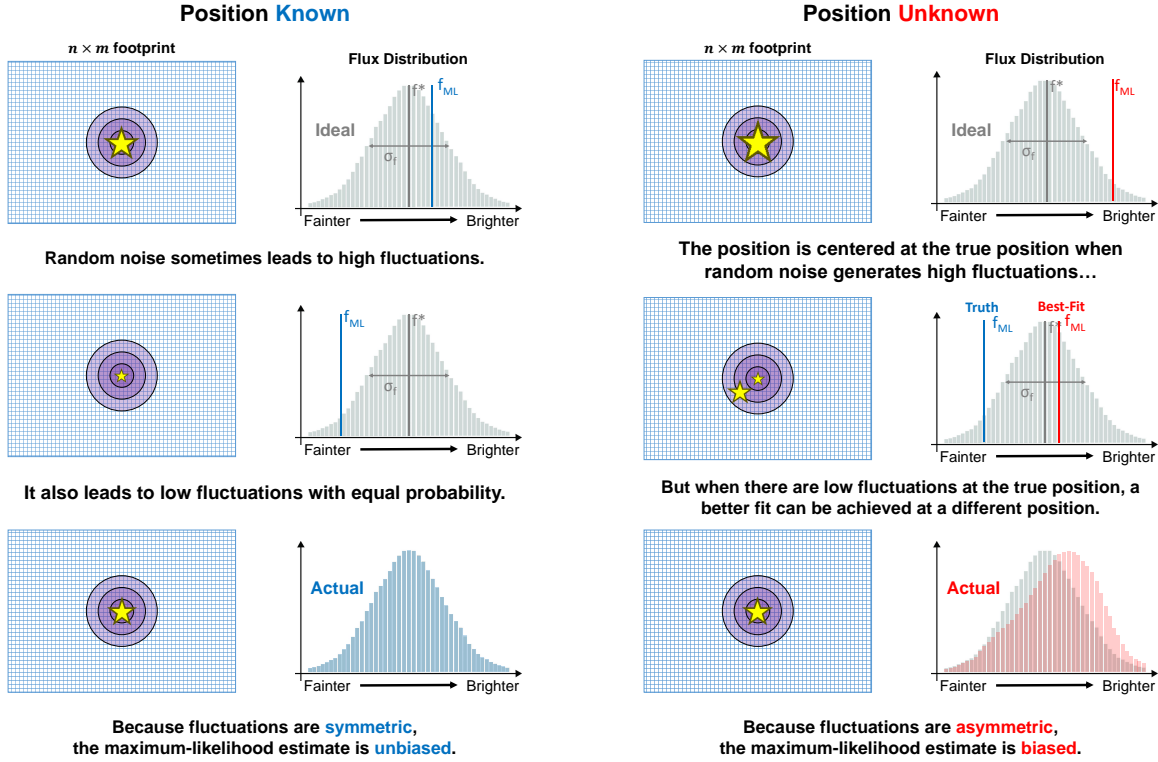


Figure 1. A schematic illustration of the bias described in §3. If the true position is known and held fixed, then random noise fluctuations tend to cause the estimated ML flux density f_{ML} to randomly fluctuate around the true value f^* with a typical dispersion of σ_f (see §2). Since these fluctuations are *symmetric*, the average estimated flux density is *unbiased*, as shown on the left in blue. Allowing the position (x, y) to vary, however, breaks this symmetry because noise fluctuations tend to draw the ML position $(x_{\text{ML}}, y_{\text{ML}})$ away from the true position (x^*, y^*) to improve the fit. This slightly biases f_{ML} against smaller values near the true position and leads to an overall *positive bias* in the estimated flux density, as shown on the right in red. This argument can be generalized to more complex models such as galaxies (see §5), which introduce additional ways in which model parameters can “soak up noise” in ways that break symmetry.

where the $Z_i \sim \mathcal{N}(0, 1)$ are again iid normal random variables. The sum of their squares represents the sum of the error-normalized residuals. We can rewrite this by recognizing that

$$\sum_{i=1}^{nm} Z_i^2 \sim \chi_A^2 \quad (24)$$

which follows a chi-square distribution with $A = nm$ degrees of freedom.

In general, we expect our best-fit parameters to “absorb” some of the scatter present in the data since we allow them to vary when we are trying to maximize the likelihood. We can make this more rigorous using **Cochran’s theorem**, which implies that the sum of error-normalized residuals for a fit with p free parameters θ will follow

$$(\hat{\mathbf{f}} - \mathbf{f}_{\theta_{\text{ML}}})^T \mathbf{C}^{-1} (\hat{\mathbf{f}} - \mathbf{f}_{\theta_{\text{ML}}}) \sim \chi_{A-p}^2 \quad (25)$$

with the sum of error-normalized residuals for the ML solution (see §4) distributed as

$$(\theta^* - \theta_{\text{ML}})^T \mathbf{C}_{\theta}^{-1} (\theta^* - \theta_{\text{ML}}) \sim \chi_p^2 \quad (26)$$

such that their combined sum leaves us with

$$(\hat{\mathbf{f}} - \mathbf{f}_{\theta_{\text{ML}}})^T \mathbf{C}^{-1} (\hat{\mathbf{f}} - \mathbf{f}_{\theta_{\text{ML}}}) + (\boldsymbol{\theta}^* - \boldsymbol{\theta}_{\text{ML}})^T \mathbf{C}_{\boldsymbol{\theta}}^{-1} (\boldsymbol{\theta}^* - \boldsymbol{\theta}_{\text{ML}}) \sim \chi_A^2 \quad (27)$$

since $\chi_i^2 + \chi_j^2 \sim \chi_{i+j}^2$.

3.2.1. Decoupled Background

There is an asymmetry between the parameters connected to modeling the object and those connected to modeling the background. When modeling an object, (f, x, y) all (in theory) can modify the model image and provide information on the scale of the PSF. Even as we increase the size of our footprint $(n \times m) \rightarrow (\infty, \infty)$, there is only a finite effective area available to constrain our PSF-based photometry model (i.e. there is a minimum variance $\sigma_{f, \text{min}}^2$ achievable set by $A_{\text{psf}}^{\text{max}}$ and σ).

In contrast, the background estimate can continually improve as the image becomes larger. This holds true for any finite-parameter background model (see Appendix B) as the size of the footprint $A \rightarrow \infty$ becomes infinitely large. This implies that there is a *fundamental difference* between “object-related” parameters and “background-related” parameters.

In the case where the area of the footprint is substantially larger than the effective area of the PSF (i.e. $A \gg A_{\text{psf}}$), we can consider the object parameters effectively decoupled from background parameters. In Appendix C, we show that the freedom in the object position parameters leads to a bias⁴ in the generalized ML flux density $f_{\text{ML}} \equiv f_{\text{ML}}(x_{\text{ML}}, y_{\text{ML}})$ relative to the ideal (unbiased) ML flux density $f_{\text{ML}}^* \equiv f_{\text{ML}}(x^*, y^*)$ in §3.1 that to leading order goes as

$$f_{\text{ML}}^* \approx f_{\text{ML}} \left(1 - \frac{X_2^2}{2} \frac{\tilde{\sigma}_{f_{\text{ML}}}^2}{f_{\text{ML}}^2} \right) \quad (28)$$

where $X_2^2 \sim \chi_2^2$ is a random variable drawn from the chi-square distribution with 2 degrees of freedom (which is determined by the 2 parameters (x, y) used to fit for the position). This has leads to a **fractional bias** of

$$\boxed{\frac{\delta_{f_{\text{ML}}}}{f_{\text{ML}}} \equiv 1 - \frac{\mathbb{E}[f_{\text{ML}}^*]}{f_{\text{ML}}} \approx \frac{\tilde{\sigma}_{f_{\text{ML}}}^2}{f_{\text{ML}}^2}} \quad (29)$$

where $\mathbb{E}[f_{\text{ML}}^*]$ is the expectation value of f_{ML}^* . This shows that f_{ML} is biased *high* relative to the true underlying flux density f^* .⁵ See Appendix C for a more detailed derivation involving higher-order terms, and D for an alternate derivation using bias tensors which will be discussed further in §5. This bias is the same as the “gradient bias” identified by Ivison et al. (2007) and the “noise bias” identified by Refregier et al. (2012).

This result gives a straightforward procedure to approximately “de-bias” f_{ML} using equation (28). Doing so, however, increases the variance in the measurement to first-order by

$$\frac{\mathbb{V}[f_{\text{ML}}^*]}{\tilde{\sigma}_{f_{\text{ML}}}^2} \approx \frac{\sigma_{f_{\text{ML}}}^2}{f_{\text{ML}}^2} \quad (30)$$

since the exact bias for any individual measurement is not known. This is an example of the **bias-variance trade-off** and leads to an increase in the total effective error following

$$\tilde{\sigma}_{f_{\text{ML}}^*} = \sqrt{\tilde{\sigma}_{f_{\text{ML}}}^2 + \mathbb{V}[f_{\text{ML}}^*]} \approx \tilde{\sigma}_{f_{\text{ML}}} \left(1 + \frac{1}{2} \frac{\mathbb{V}[f_{\text{ML}}^*]}{\tilde{\sigma}_{f_{\text{ML}}}^2} \right) = \boxed{\tilde{\sigma}_{f_{\text{ML}}} \left(1 + \frac{1}{2} \frac{\tilde{\sigma}_{f_{\text{ML}}}^2}{f_{\text{ML}}^2} \right)} \quad (31)$$

The magnitude of this bias for PSF photometry is generally small but not totally negligible: a nominally 10σ source (i.e. $f_{\text{ML}} = 10\tilde{\sigma}_{f_{\text{ML}}}$) incurs a 1% bias and 0.5% error underestimate. We will return to this in §5 when we examine the behavior of f_{ML} when modeling extended objects.

⁴ Note that this effect is completely independent of (and unrelated to) selection effects such as Malmquist bias that can also cause sources to naturally be biased high close to detection limits/cutoffs. It is also independent of Eddington bias, which causes the number of bright objects to be overestimated when faint objects are more common than bright ones.

⁵ While the ML flux density f_{ML} is a biased estimator of the true flux f^* , the *mean* flux density f_{mean} (derived from, e.g., Markov Chain Monte Carlo methods) is in fact an *unbiased* estimator of the true flux, to order SNR^{-2} . See Appendix E for more details.

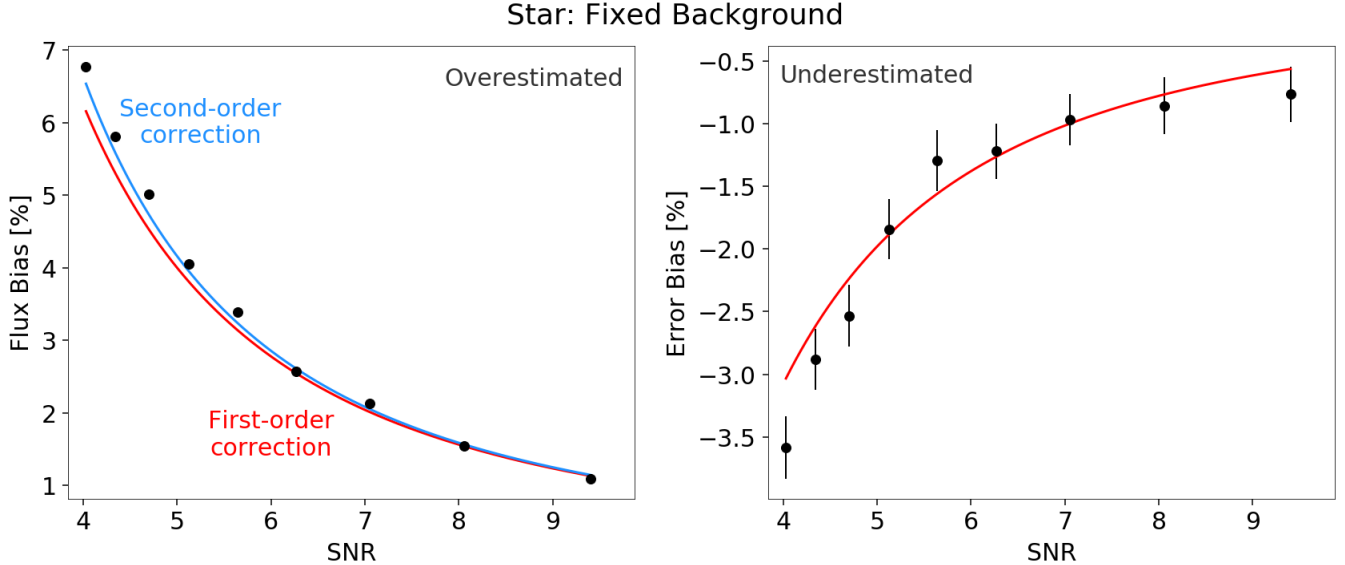


Figure 2. **Left:** The bias in the estimated maximum-likelihood flux density for a point source assuming a fixed background relative to the true value. First (red) and second-order (blue) analytic predictions (Appendix C) are compared with results from simulated images. The flux estimate is biased high because the position parameters will move to better fit the noise in the data, increasing the log-likelihood and estimated flux. To leading order in SNR, the fractional flux bias is SNR^{-2} . **Right:** The bias in the derived errors after correcting for the mean bias in the ML flux. Since the exact bias for any individual measurement is not known, subtracting the average bias increases the error by $1/2 \times \text{SNR}^{-2}$. This is an example of the *bias-variance tradeoff* where decreasing the bias increases the variance.

We test our analytic predictions by creating a set of simulated point-source images and running maximum-likelihood photometry on them. Our simulated images have a point-source with a circular Gaussian PSF of $\sigma = 2$ pixels in the center of a 101×101 pixel image with iid Gaussian noise in each pixel. We simulate sources of nine fluxes ranging from 4.0σ to 9.4σ , evenly spaced in $1/\text{SNR}$. For each flux, we create 100,000 different simulated images. Figure 2 shows that the mean flux bias and flux errors from these simulated images agree well with our predictions.

It is crucial to note this bias *does not* by itself arise from the fact that ML estimators tend to “overfit” the data based on the number of free parameters relative to the truth. If that were the case, we should not have found that the ML estimate at the true position f_{ML}^* was actually unbiased. Instead, this bias arises because of the *way* in which this overfitting occurs. At the true position, f_{ML}^* is allowed to chase noise peaks, but it does so in a symmetrical way: the noise fluctuations in the image are symmetric, and so f_{ML}^* is just as likely to fluctuate upwards relative to f^* as it is to fluctuate downwards. Once the position (x, y) is allowed to vary, however, the model can move the source to chase the noise. This breaks the symmetry from earlier: the source will tend to stay in the correct position with an overestimated f_{ML} when the noise fluctuates upwards around the true position (x^*, y^*) , but will try to chase the noise when the noise fluctuates downwards around (x^*, y^*) . This position-dependent behavior of f_{ML} is broadly illustrated in Figure 1 and shown in more detail in Figures 3 and 4. Averaging over this behavior as a function of position then gives the results derived above.

3.2.2. Coupled Background

The result we derived above holds if the image is sufficiently large that background estimation is effectively decoupled from modeling the actual object. In the case where this is not true (i.e. $A \not\gg A_{\text{psf}}$), we instead need to consider how background estimation is covariant with our model parameters. The mixed 2nd-order derivatives of the log-likelihood give

$$\partial_f \partial_b \ln \mathcal{L}(x, y) = -\frac{1}{\sigma^2} \sum_i p_i(x, y) = -\frac{1}{\sigma^2} \quad (32)$$

$$\partial_x \partial_b \ln \mathcal{L}(x, y) = -\frac{f}{\sigma^2} \sum_i \partial_x p_i(x, y) \approx 0 \quad (33)$$

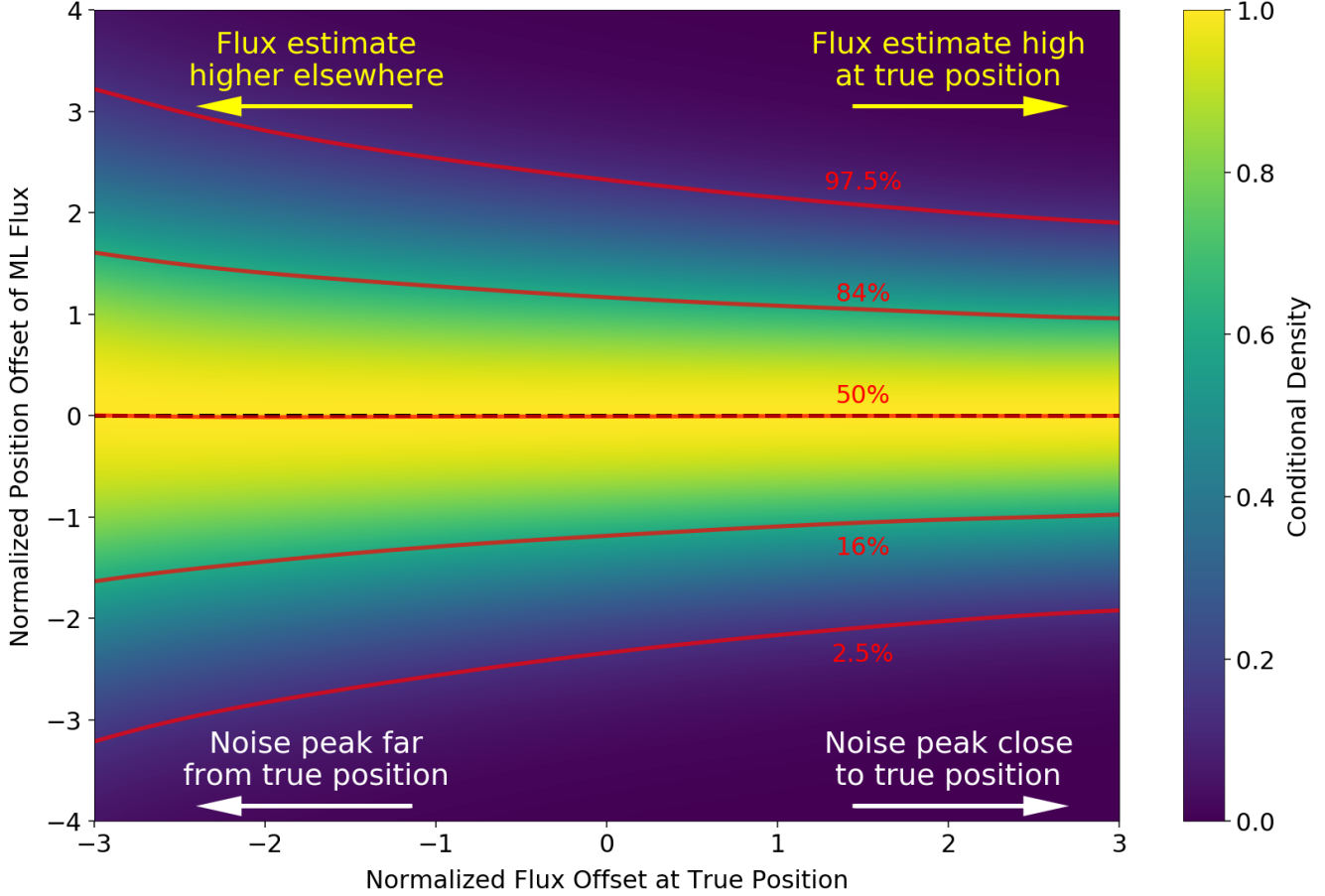


Figure 3. An illustration of the “centering bias” described in Figure 1. When random fluctuations lead to “noise peaks” near the true position (right), the maximum-likelihood position $(x_{\text{ML}}, y_{\text{ML}})$ will remain close to the true position (x^*, y^*) (smaller dispersion) but the flux density f_{ML} will be overestimated. When random fluctuations generate noise peaks further from the true position, however, the fit follows them away from the true position (larger dispersion). This leads $f_{\text{ML}}(x_{\text{ML}}, y_{\text{ML}})$ at the maximum-likelihood position to generally be larger than the $f_{\text{ML}}(x^*, y^*)$ that *would be* estimated at the true position (left). The general behavior in Figure 2 describing the mean bias (shown in purple) arises from averaging over these two behaviors.

assuming that $p_i(x, y)$ is oversampled and roughly symmetric in x (see §4.3). As shown in §4.2, the contribution from the mixed partial with respect to f and b is expected to contribute to a fractional underestimate of the variance proportional to the ratio A/A_{psf} of the area of the footprint versus the effective area of the PSF. This gives a modified variance of

$$\sigma_f^2(x, y) = \frac{A_{\text{psf}}(x, y) \times \sigma^2}{1 - \frac{A_{\text{psf}}(x, y)}{A}} = \frac{A}{A - A_{\text{psf}}(x, y)} \times \tilde{\sigma}_f^2 \quad (34)$$

since by construction $A \geq A_{\text{psf}}$. Note that we have dropped $\tilde{\sigma}_f$ since σ_f is now the “true” uncertainty of our ML estimator that takes into account the relative coupling between the ML background estimate b_{ML} and the parameters used to model our object $(f_{\text{ML}}, x_{\text{ML}}, y_{\text{ML}})$.

Substituting in σ_f for $\tilde{\sigma}_f$ into our expressions from §3.2.1 then modifies the effective SNR to give

$$\boxed{\frac{\delta_{f_{\text{ML}}}}{f_{\text{ML}}} \approx \frac{\sigma_{f_{\text{ML}}}^2}{f_{\text{ML}}^2}, \quad \frac{\mathbb{V}[f_{\text{ML}}^*]}{\sigma_{f_{\text{ML}}}^2} \approx \frac{\sigma_{f_{\text{ML}}}^2}{f_{\text{ML}}^2}} \quad (35)$$

When the effective size of the footprint is large compared to the PSF, then $A/(A - A_{\text{psf}}) \rightarrow 1$ and the background is effectively decoupled from the modeling of the object, leading to our results in §3.2.1. When the effective size becomes more comparable to the PSF, then $A/(A - A_{\text{psf}}) \rightarrow \infty$ and the covariance between the background and flux density dominate the error budget. This has the effect of increasing the expected bias by decreasing the effective SNR.

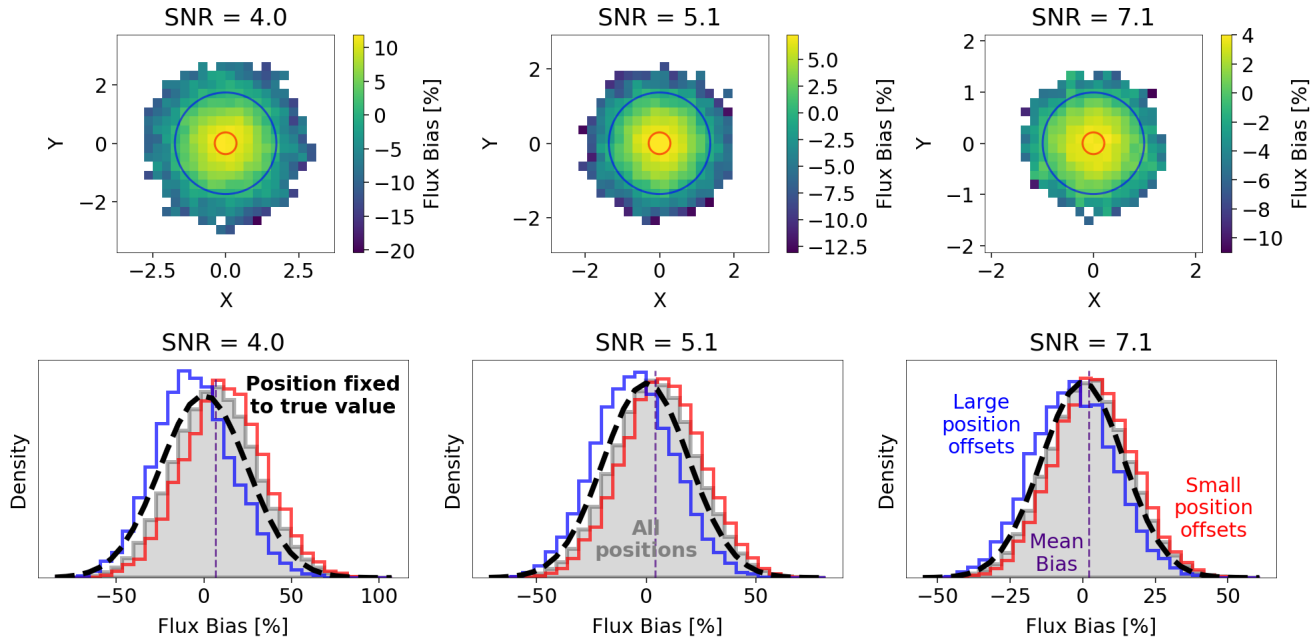


Figure 4. The impact of “centering bias” on the estimated maximum-likelihood flux density f_{ML} as a function of signal-to-noise ratio (SNR). **Top:** The bias in f_{ML} for a point source, assuming a fixed background, relative to the true value as a function of position (x, y) at various signal-to-noise ratios (SNR). In all cases, f_{ML} is biased high near the true position and low at the outskirts with amplitudes based on the SNR. **Bottom:** The corresponding distribution of f_{ML} across all positions (gray) compared with those with small position offsets (red, extracted inside the red circles in the top panels) and large position offsets (blue, extracted outside the blue circles in the top panels). The (unbiased) distribution that would arise if the position (x, y) was fixed to the true value (x^*, y^*) is shown as the thick black dashed curve. Because the position is left free, the fit is allowed to chase noise fluctuations away from the true position whenever noise fluctuations would tend to lead to smaller inferred f_{ML} at a given position. This systematically “removes” low f_{ML} estimates derived near the true position, which are subsequently biased high. At larger position offsets, the model has less overlap with the true PSF, which in general biases f_{ML} low. The general behavior in Figure 2 describing the mean bias (shown in purple) arises from averaging over these two behaviors.

We augment the set of simulation images used to generate Figure 2 by considering five different image sizes approximately evenly distributed in $1/A$: 11, 13, 15, 23, and 101 pixels. The effective SNR of a given flux will decrease as image size decreases. In Figure 5, we show that our analytic predictions in terms of the effective SNR hold in these simulated images.

We want to note that while this effect is conceptually useful going forward, in practice the impact is extremely small. For instance, in SDSS the background is determined in patches of 256×256 pixels.⁶ With a median seeing of $1.32''$ in r band⁷ and pixel size of $0.4''$ (Gunn et al. 1998), $A_{\text{psf}}/A = 4.4 \times 10^{-4}$. Similarly, in LSST the background will be determined in patches of 256×256 or 512×512 pixels.⁸ With a median seeing of $0.7''$ in r band and pixel size of $0.2''$ (LSST Science Collaboration et al. 2009), $A_{\text{psf}}/A = 4.3 \times 10^{-4}$ if the background is determined using 256×256 pixel patches. A significantly larger effect is present in unWISE (Schlafly et al. 2019), which estimates the sky background in much smaller (20×20) pixel regions: with a PSF FWHM of $6''$ and a pixel scale of $2.75''$ (Wright et al. 2010), $A_{\text{psf}}/A = 2.8\%$.

4. ERRORS

The naive uncertainty estimates $\tilde{\sigma}_f$ derived in §2 and utilized in most of §3 only are equal to the *true* uncertainties σ_f if there is no covariance between the $p \times 1$ parameter vector θ that comprises our model. In general, we can assume the likelihood is approximately multivariate normal so that

$$\theta_{\text{true}} \sim \mathcal{N}(\theta_{\text{ML}}, \mathbf{C}_\theta(\theta_{\text{ML}})) \quad (36)$$

⁶ <https://www.sdss.org/dr14/algorithms/sky/>

⁷ https://www.sdss.org/dr14/imaging/other_info/

⁸ <https://confluence.lsstcorp.org/display/LSWUG/Measurement+in+the+LSST+Stack>

Star: Variable Background

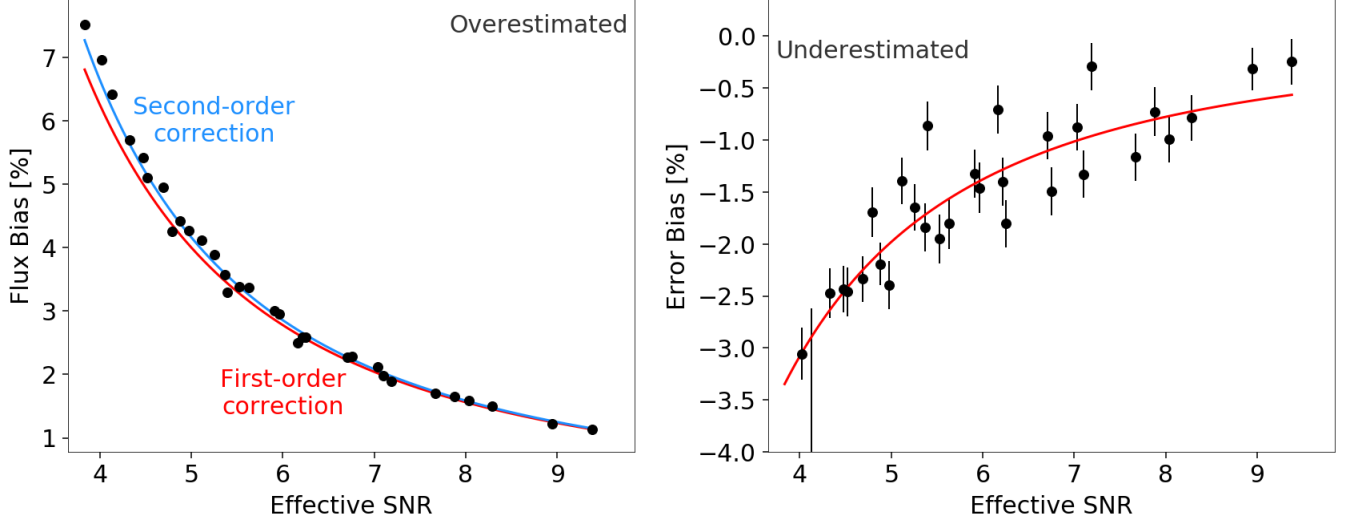


Figure 5. As Figure 2, but now with a variable background and computed over various image sizes. The effective signal-to-noise ratios (SNRs) decrease due to the covariance between the background and the estimated flux density as described in §3.2.2, which depend on the relative size of the image A compared to the effective size of the point-spread function A_{psf} . The analytic predictions computed using these lower effective SNRs still model the data well.

where θ_{ML} is the ML estimator. Following the discussion in §2 (see also Appendix C), we can estimate the covariance around the ML solution as

$$\mathbf{C}_{\theta}(\theta_{\text{ML}}) \approx -\mathbb{E}_{\mathbf{D}} [\partial_{\theta}^2 \ln \mathcal{L}(\theta_{\text{ML}}) | \theta_{\text{ML}}]^{-1} \equiv (\mathcal{F}_{\theta}(\theta_{\text{ML}}))^{-1} = -(\partial_{\theta}^2 \ln \mathcal{L}(\theta_{\text{ML}}))^{-1} \quad (37)$$

Here, $\mathbb{E}_{\mathbf{D}}[\cdot | \theta_{\text{ML}}]$ is the expectation value (i.e. mean) with respect to (random realizations of) the data \mathbf{D} with θ_{ML} fixed. $\partial_{\theta} \ln \mathcal{L}$ represents the $p \times 1$ Jacobian vector with respect to θ with elements $(\partial_{\theta} \ln \mathcal{L})_i = \partial_{\theta_i} \ln \mathcal{L}$, $\partial_{\theta}^2 \ln \mathcal{L}$ represents the $p \times p$ Hessian matrix whose elements are comprised of the second-order derivatives of the log-likelihood $(\partial_{\theta}^2 \ln \mathcal{L})_{ij} = \partial_{\theta_i} \partial_{\theta_j} \ln \mathcal{L}$, and $\mathcal{F}_{\theta}(\theta_{\text{ML}})$ is the **Fisher Information Matrix (FIM)** evaluated at θ_{ML} . The final equality, where we remove the expectation value and equate the FIM with the inverse of the Hessian, follows from our assumption that the likelihood is multivariate normal.

With this more general result, we see that the results derived in §2 for the associated marginal uncertainties on each parameter $\tilde{\sigma}$ only are equal to the true marginal uncertainties σ when the FIM is diagonal. When the off-diagonal elements of the FIM (i.e. mixed derivatives) are non-zero, the actual marginal uncertainties along the diagonal of $\mathbf{C}_{\theta}(\theta_{\text{ML}})$ for the ML solution are larger. In this section, we examine the special 2×2 case involving just the flux density f and one other parameter θ_i for illustrative purposes.

4.1. Error Underestimation in Two-Parameter Models

In the special case where the FIM is 2×2 , the inverse has a simple analytic form of

$$\begin{aligned} \mathbf{C}_{\theta}(\theta_{\text{ML}}) &= [\mathcal{F}_{\theta}(\theta_{\text{ML}})]^{-1} = - \begin{bmatrix} \partial_{\theta_i}^2 \ln \mathcal{L}(\theta_{\text{ML}}) & \partial_{\theta_i} \partial_{\theta_j} \ln \mathcal{L}(\theta_{\text{ML}}) \\ \partial_{\theta_i} \partial_{\theta_j} \ln \mathcal{L}(\theta_{\text{ML}}) & \partial_{\theta_j}^2 \ln \mathcal{L}(\theta_{\text{ML}}) \end{bmatrix}^{-1} \\ &= \frac{1}{\det(\mathcal{F}_{\theta}(\theta_{\text{ML}}))} \begin{bmatrix} -\partial_{\theta_j}^2 \ln \mathcal{L}(\theta_{\text{ML}}) & \partial_{\theta_i} \partial_{\theta_j} \ln \mathcal{L}(\theta_{\text{ML}}) \\ \partial_{\theta_i} \partial_{\theta_j} \ln \mathcal{L}(\theta_{\text{ML}}) & -\partial_{\theta_i}^2 \ln \mathcal{L}(\theta_{\text{ML}}) \end{bmatrix} \end{aligned} \quad (38)$$

where the determinant is

$$\det(\mathcal{F}_{\theta}(\theta_{\text{ML}})) = \partial_{\theta_i}^2 \ln \mathcal{L}(\theta_{\text{ML}}) \partial_{\theta_j}^2 \ln \mathcal{L}(\theta_{\text{ML}}) - (\partial_{\theta_i} \partial_{\theta_j} \ln \mathcal{L}(\theta_{\text{ML}}))^2 \quad (39)$$

When ignoring the covariances, the cross-terms vanish and the naive error estimate for θ_i reduces to

$$\tilde{\sigma}_{\theta_i}^2(\theta_{\text{ML}}) = -(\partial_{\theta_i}^2 \ln \mathcal{L}(\theta_{\text{ML}}))^{-1} \quad (40)$$

which is identical to our results from §2. Properly including the covariance instead gives

$$\sigma_{\theta_i}^2(\boldsymbol{\theta}_{\text{ML}}) = \frac{-\partial_{\theta_j}^2 \ln \mathcal{L}(\boldsymbol{\theta}_{\text{ML}})}{\partial_{\theta_i}^2 \ln \mathcal{L}(\boldsymbol{\theta}_{\text{ML}}) \partial_{\theta_j}^2 \ln \mathcal{L}(\boldsymbol{\theta}_{\text{ML}}) - (\partial_{\theta_i} \partial_{\theta_j} \ln \mathcal{L}(\boldsymbol{\theta}_{\text{ML}}))^2} \quad (41)$$

The ratio of the naive estimate to the true estimate of the variance is

$$\frac{\tilde{\sigma}_{\theta_i}^2(\boldsymbol{\theta}_{\text{ML}})}{\sigma_{\theta_i}^2(\boldsymbol{\theta}_{\text{ML}})} = \frac{\partial_{\theta_i}^2 \ln \mathcal{L}(\boldsymbol{\theta}_{\text{ML}}) \partial_{\theta_j}^2 \ln \mathcal{L}(\boldsymbol{\theta}_{\text{ML}}) - (\partial_{\theta_i} \partial_{\theta_j} \ln \mathcal{L}(\boldsymbol{\theta}_{\text{ML}}))^2}{\partial_{\theta_i}^2 \ln \mathcal{L}(\boldsymbol{\theta}_{\text{ML}}) \partial_{\theta_j}^2 \ln \mathcal{L}(\boldsymbol{\theta}_{\text{ML}})} = 1 - \frac{(\partial_{\theta_i} \partial_{\theta_j} \ln \mathcal{L}(\boldsymbol{\theta}_{\text{ML}}))^2}{\partial_{\theta_i}^2 \ln \mathcal{L}(\boldsymbol{\theta}_{\text{ML}}) \partial_{\theta_j}^2 \ln \mathcal{L}(\boldsymbol{\theta}_{\text{ML}})} \quad (42)$$

This gives a fractional bias of

$$\boxed{\frac{\delta_{\tilde{\sigma}_{\theta_i}^2}}{\sigma_{\theta_i}^2}(\boldsymbol{\theta}_{\text{ML}}) \equiv \frac{\tilde{\sigma}_{\theta_i}^2(\boldsymbol{\theta}_{\text{ML}})}{\sigma_{\theta_i}^2(\boldsymbol{\theta}_{\text{ML}})} - 1 = -\frac{(\partial_{\theta_i} \partial_{\theta_j} \ln \mathcal{L}(\boldsymbol{\theta}_{\text{ML}}))^2}{\partial_{\theta_i}^2 \ln \mathcal{L}(\boldsymbol{\theta}_{\text{ML}}) \partial_{\theta_j}^2 \ln \mathcal{L}(\boldsymbol{\theta}_{\text{ML}})}} \quad (43)$$

This is defined to be negative to indicate that we're dealing with underestimates rather than overestimates.⁹

This result – where the error underestimates are the ratio of the product of the “interaction” terms divided by the “naive” terms – provides a quick and intuitive way to estimate how covariances among parameters impact our marginalized error estimates.¹⁰ In the case where there is no covariance among the parameters, $\delta_{\tilde{\sigma}_f^2}/\sigma_f^2 = 0$ and $\tilde{\sigma}_f^2 = \sigma_f^2$. In the case where our parameters become perfectly degenerate, we instead get $\delta_{\tilde{\sigma}_f^2}/\sigma_f^2 \rightarrow 1$ and $\tilde{\sigma}_f^2/\sigma_f^2 \rightarrow \infty$.

4.2. Background Covariance

As an example, consider that we fix the position (x, y) of the source and are jointly estimating the flux density f and sky background b . The mixed f and b derivative is

$$\partial_f \partial_b \ln \mathcal{L}(x, y) = -\frac{1}{\sigma^2} \sum_i p_i(x, y) = -\frac{1}{\sigma^2} \quad (44)$$

which is insensitive to the value of f and b . This then gives

$$\mathcal{F}_{\boldsymbol{\theta}}(x, y) = -\frac{1}{\sigma^2} \begin{bmatrix} A_{\text{psf}}(x, y) & 1 \\ 1 & A \end{bmatrix} \quad (45)$$

where again $A_{\text{psf}}(x, y) = \sum_i p_i^2(x, y)$ and $A = nm$. This in turn gives

$$\mathbf{C}_{\boldsymbol{\theta}}(x, y) = \frac{\sigma^2}{AA_{\text{psf}}(x, y) - 1} \begin{bmatrix} A & -1 \\ -1 & A_{\text{psf}}(x, y) \end{bmatrix} \quad (46)$$

This means the naive errors $\tilde{\sigma}_f^2$ we previously derived, which ignored the covariance between the flux and the background, are smaller than the actual uncertainties by a factor

$$\boxed{\frac{\delta_{\tilde{\sigma}_f^2}}{\sigma_f^2}(x, y) = -\frac{A_{\text{psf}}(x, y)}{A}} \quad (47)$$

This is the result used in §3.2.2.

4.3. Position Covariance

The mixed partial derivative of the log-likelihood with respect to f and one coordinate of the position, say, x , is

$$\partial_f \partial_x \ln \mathcal{L}(x, y, f, b) = \frac{1}{\sigma^2} \sum_i \left(\hat{f}_i - b - fp_i(x, y) - fp_i(x, y) \right) \partial_x p_i(x, y) \quad (48)$$

⁹ This is a consequence of the fact that $(\partial_{\theta_i} \partial_{\theta_j} \ln \mathcal{L})^2 \leq (\partial_{\theta_i}^2 \ln \mathcal{L})(\partial_{\theta_j}^2 \ln \mathcal{L})$, which arises from the Cauchy-Schwarz inequality.

¹⁰ Unfortunately, this intuition does not generalize to larger matrices.

In the case where $\mathbf{p}_{x,y}$ is approximately symmetric (even) in x , the derivative $\partial_x \mathbf{p}_{x,y}$ will be approximately antisymmetric (odd) in x . We would then expect

$$\sum_i p_i(x,y) \partial_x p_i(x,y) \approx \iint p(x,y) \partial_x p(x,y) dx dy = 0 \quad (49)$$

assuming that (1) the PSF is oversampled so that our sum over pixels is a reasonable approximation to the integral and (2) the impact of sub-pixel shifts is small. If our PSF is undersampled so that it occupies only a few pixels, then this term may be significantly non-zero. Note that the behavior under any general covariance matrix is not guaranteed to be small even if the PSF is oversampled, although in most practical applications where only nearby pixels are correlated with each other this behavior still tends to hold.

If our model $(x_{\text{ML}}, y_{\text{ML}}, f_{\text{ML}})$ is close to the truth, we expect the residuals $\hat{\mathbf{f}} - \mathbf{b} - f\mathbf{p}(x,y)$ to be roughly distributed following a multivariate Normal, which we will write as

$$\mathbf{X} \sim \mathbf{C}^{1/2} \mathbf{Z} \sim \mathcal{N}(\mathbf{0}, \mathbf{C}) \quad (50)$$

where \mathbf{Z} is an $mn \times 1$ iid normal **random vector** and $\mathbf{C}^{1/2}$ is the symmetric square root of the covariance matrix \mathbf{C} . This implies that the residual contribution to our flux density-position covariance should be roughly distributed as

$$\left(\mathbf{C}^{1/2} \mathbf{Z} \right)^T \mathbf{C}^{-1} \partial_x \mathbf{p}_{x,y} = \mathbf{Z}^T \mathbf{C}^{-1/2} \partial_x \mathbf{p}_{x,y} \quad (51)$$

Since the expectation value $\mathbb{E}[\mathbf{Z}^T \mathbf{Y}] = \mathbb{E}[\mathbf{Z}]^T \mathbf{Y} = \mathbf{0}$ for a normal random vector given any fixed matrix \mathbf{Y} , our FIM reduces to

$$\mathcal{F}_{\theta}(x_{\text{ML}}, y_{\text{ML}}, f_{\text{ML}}) \approx -\frac{1}{\sigma^2} \begin{bmatrix} \sum_i p_i^2(x_{\text{ML}}, y_{\text{ML}}) & 0 \\ 0 & f_{\text{ML}}^2 \sum_i (\partial_x p_i(x_{\text{ML}}, y_{\text{ML}}))^2 \end{bmatrix} \quad (52)$$

and

$$\boxed{\frac{\delta_{\sigma_f^2}}{\sigma_f^2}(x_{\text{ML}}, y_{\text{ML}}, f_{\text{ML}}) \approx 0} \quad (53)$$

This implies that while modeling the position biases the mean value of the ML flux density estimate $f_{\text{ML}}(x_{\text{ML}}, y_{\text{ML}})$ as discussed in §3, it *does not* impact the associated error estimates.

5. GALAXIES

In general, our results from §3.2 (see also Appendix C) can be generalized to a p -parameter object model to give

$$f_{\text{ML}}^* \approx f_{\text{ML}} \left[1 - \frac{X_{p-1}^2}{2} \frac{\sigma_{f_{\text{ML}}}^2}{f_{\text{ML}}^2} \right] \quad (54)$$

where $X_{p-1}^2 \sim \chi_{p-1}^2$ is a chi-square random variable with $p-1$ degrees of freedom, $\sigma_{f_{\text{ML}}}^2$ is the “true” error estimate that includes the covariances from the other object parameters as well as the background (see §4), and the $p-1$ comes from the fact that we are excluding the flux density f . This gives

$$\boxed{\frac{\delta_{f_{\text{ML}}}}{f_{\text{ML}}} \approx \frac{p-1}{2} \frac{\sigma_{f_{\text{ML}}}^2}{f_{\text{ML}}^2}, \quad \frac{\mathbb{V}[f_{\text{ML}}^*]}{\sigma_{f_{\text{ML}}}^2} \approx \frac{p^2 - 4p + 7}{4} \frac{\sigma_{f_{\text{ML}}}^2}{f_{\text{ML}}^2}} \quad (55)$$

Galaxies thus increase the bias and underestimate the variance both by including more free parameters (increasing p) as well as by introducing covariances among them (increasing $\sigma_{f_{\text{ML}}}^2$).

Let’s first consider the PSF photometry case used to fit stars (point sources). In that instance, we introduce two additional free model parameters (x, y) used to model the position of our source and one (b) to model the background. This gives a bias that goes as $(p-1)/2 = 2/2 = 1 \times \text{SNR}^{-2}$. In addition, because there is no covariance between the position (x, y) of our source and the flux density f (see §4.3), the true variance σ_f^2 is only inflated by a factor of $A/(A - A_{\text{psf}})$ due to the covariance with the background.

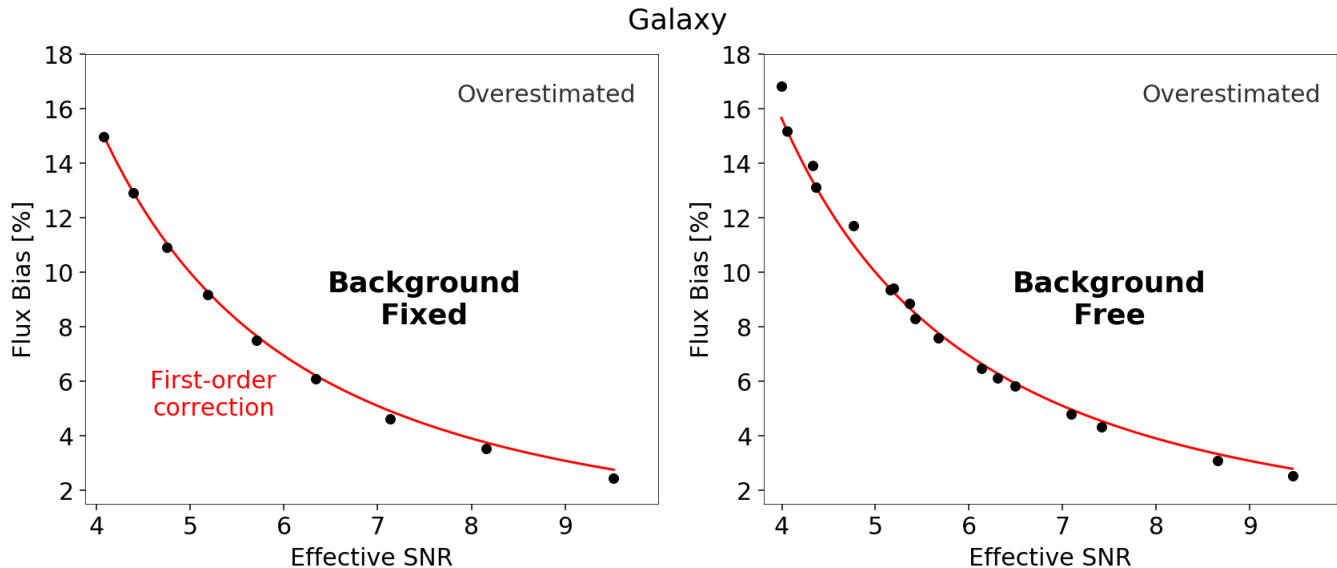


Figure 6. The bias in the estimated maximum-likelihood flux density f_{ML} for a 2-D “Gaussian galaxy” assuming a fixed (left) and varying (right) background over several image sizes. The first-order analytic predictions (Appendix C) are shown in red. f_{ML} is biased higher than in the point-source case from Figure 2 because the shape parameters can “absorb” additional noise in the image, further increasing the log-likelihood and estimated flux. To leading order, the fractional flux bias is $5/2 \times \text{SNR}^{-2}$.

By contrast, when modeling galaxies using single-component models (e.g. Sersic profiles), we are typically introducing anywhere from 1-4 additional parameters beyond just position (x, y) and flux density f . These at a minimum often include parameters to model the physical size (e.g., effective radius R_e), elongated shapes/projection effects (e.g., axis ratio b/a and position angle ϕ), and surface brightness profiles (e.g., scale index n). For multi-component models such as `cmode1` (Abazajian et al. 2004), this can include up to 8 additional parameters.

Due to the additional parameters involved, we should expect the ML flux density estimates for galaxies (and other extended objects) to *at least* double since the number of free parameters (besides f) can go from 2 to 4 – 10. In addition, because galaxy models can introduce potentially strong covariances between f and other model parameters, we would expect σ_f^2 to increase even in the absence of any background modeling by *at least* a factor of a few. If we include the background, we would expect σ_f^2 to increase *even further* since the galaxy increases the “effective PSF area” A_{psf} as it is functionally equivalent to a point source with an “effective PSF” that is the convolution of the original PSF with the extended galaxy model.

These combined effects (larger effective image areas, more parameters, and stronger parameter covariances) imply that we expect biases arising purely from our ML approach to now be roughly 0.6% at 20σ , 2.5% at 10σ , and 10% at 5σ .

5.1. Gaussian Galaxy with Known Shape Parameters

To illustrate the impact of these three features directly (more free parameters, additional parameter covariances, enlarged effective PSF), we will derive results explicitly below for a circular Gaussian PSF with variance s^2 and a 2-D Gaussian galaxy model with semi-major/semi-minor axes s_1/s_2 and position angle ϕ . Without loss of generality, we will take the true $\phi^* = 0$ to simplify our calculations since it doesn’t affect the size of the galaxy. These results build on those from Condon (1997) and Refregier et al. (2012).

For a point source, the effective PSF area is

$$A_{\text{psf}} = \sum_i p_i^2(x, y) \rightarrow 4\pi s^2 \quad (56)$$

in the limit where the footprint is sufficiently large and the PSF is oversampled. For a Gaussian galaxy convolved with our PSF, however, this increases to

$$A_{\text{psf}} \rightarrow 4\pi \sqrt{(s_1^2 + s^2)(s_2^2 + s^2)} \equiv 4\pi a_1 a_2 \quad (57)$$

where a_1 and a_2 are now the PSF-convolved semi-major and semi-minor axes, respectively. Assuming that $a_1 = a_1^*$, $a_2 = a_2^*$, and $\phi = \phi^*$ are *known and fixed* to their true values, this would increase the underlying bias by

$$\frac{\delta_{f_{\text{ML}}}}{f_{\text{ML}}} \approx \frac{2}{2} \frac{\sigma_{f_{\text{ML}}}^2}{f_{\text{ML}}^2} = \frac{1}{1 - \frac{A_{\text{psf}}}{A}} \frac{\tilde{\sigma}_{f_{\text{ML}}}^2}{f_{\text{ML}}^2} = \frac{A_{\text{psf}}}{1 - \frac{A_{\text{psf}}}{A}} \frac{\sigma^2}{f_{\text{ML}}^2} \quad (58)$$

where δ_f/f is again the fractional bias and σ^2 is again the variance of the normal iid noise in the footprint. At fixed SNR, this then implies

$$\frac{\delta_{f_{\text{ML}}}}{f_{\text{ML}}}(a_1^*, a_2^*, \phi^*, A) = \frac{A_{\text{psf}}(a_1^*, a_2^*)}{1 - \frac{A_{\text{psf}}(a_1^*, a_2^*)}{A}} \frac{\sigma^2}{f_{\text{ML}}^2} = \frac{4\pi a_1^* a_2^*}{1 - \frac{4\pi a_1^* a_2^*}{A}} \frac{\sigma^2}{f_{\text{ML}}^2} \quad (59)$$

5.2. Gaussian Galaxy with Unknown Shape Parameters

While the case above is instructive, it is not representative of the typical case where a_1 , a_2 , and ϕ are left free when searching for a ML solution. As shown in Appendix F, the impact of the additional covariances among the parameters causes the uncertainties to increase such that

$$\frac{\sigma_f^2}{\sigma^2} = \frac{(\mathcal{F}^{-1})_{ff}}{\sigma^2} \approx \frac{8\pi a_1 a_2}{1 - \frac{8\pi a_1 a_2}{A}} = \boxed{\frac{2A_{\text{psf}}}{1 - \frac{2A_{\text{psf}}}{A}}} \quad (60)$$

essentially doubling the effective PSF area. This, along with the additional three free parameters, leads to a bias of

$$\boxed{\frac{\delta_{f_{\text{ML}}}}{f_{\text{ML}}} = \frac{5}{2} \frac{8\pi a_{1,\text{ML}} a_{2,\text{ML}}}{1 - \frac{8\pi a_{1,\text{ML}} a_{2,\text{ML}}}{A}} \frac{\sigma^2}{f_{\text{ML}}^2}} \quad (61)$$

We created a set of simulated images of a 2D Gaussian galaxy and run maximum-likelihood photometry on them, with s_1 , s_2 , and ϕ as free parameters. Our simulated images have a circular Gaussian galaxy of $s_1 = s_2 = 1$ pixel with a circular Gaussian PSF of $\sigma = 2$ pixels. Again, each pixel has iid Gaussian noise. For the fixed-background case, we simulate sources of nine fluxes ranging from 4.3σ to 10.0σ , evenly spaced in $1/\text{SNR}$. For the free background case, we consider the same fluxes in the previously used five image sizes (11, 13, 15, 23, and 101 pixels). Again, we create 100,000 different simulated images for each configuration. Figure 6 shows that the mean flux bias from the simulated galaxy images agree well with our predictions in both the fixed background and free background case.

Although we have focused on flux density estimates, we note that Refregier et al. (2012) have also examined a similar bias in derived galaxy shapes and sizes.¹¹ We encourage interested readers to examine their work for additional details.

6. EXTENSION TO MULTI-BAND FITTING

We now examine the case where an object is modeled in multiple bands. We will consider two cases. The first (§6.1) is where the object is “detected” in a single band, after which the position is fixed when across all the bands. This is analogous to surveys such as SDSS, which “detected” sources in the r -band. The second (§6.2) is where the object is modeled simultaneously across all bands. This is somewhat equivalent to most modern surveys, which “detect” an object in a stacked (PSF-matched) image constructed from all the bands.

6.1. Single-band Detection

Let’s assume that our object is detected in band D , after which the ML position $(x_{\text{ML}}, y_{\text{ML}}) = (x_D^{\text{ML}}, y_D^{\text{ML}}) \equiv (x_D, y_D)$ is fixed. As shown in §3, we expect that the ML flux density estimate in this band to be overestimated by an amount based on the PSF-normalized SNR. Following our previous assumption that the likelihood is multivariate normal around the ML parameters θ_{ML} , we would expect the values for our ML flux density estimates $f_{j,\text{ML}}$ in other band $j \neq D$ to be

$$f_{j,\text{ML}}(x_D, y_D, b_j^*) \approx \frac{\sum_i (f_k^* p_i(x^*, y^*) + \sigma_j Z_i) p_i(x_D, y_D)}{\sum_i p_i^2(x_D, y_D)} \quad (62)$$

where Z_i is again an iid normally distributed random variable, σ_j is the noise in band j , and we have again assumed that background b_j is known and fixed to the true value b_j^* . This result is analogous to equation (20), except that we have assumed a mismatch in the position between our model at (x_D, y_D) and the source at (x^*, y^*) .

¹¹ They also derive a bias in the estimated flux density which agrees with our results.

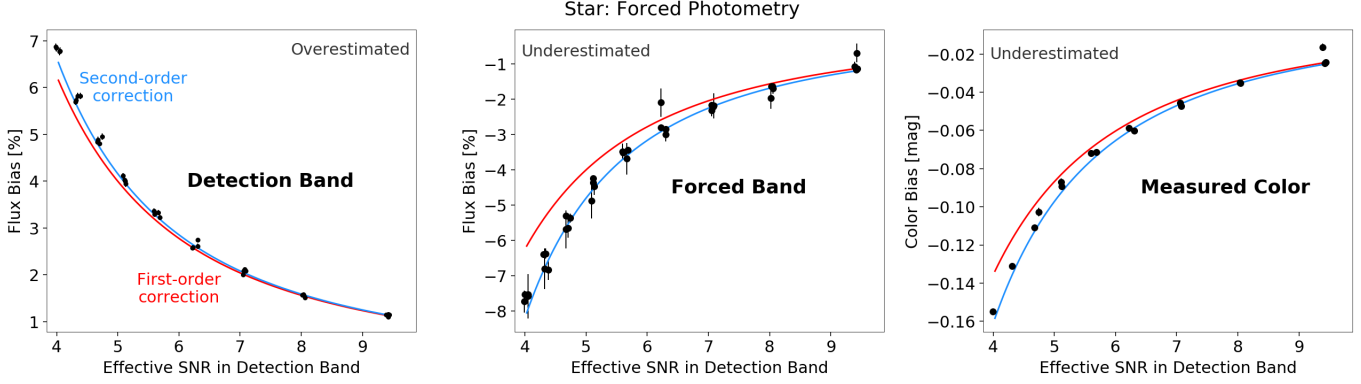


Figure 7. The bias in the estimated maximum-likelihood flux density for a point source assuming a fixed background relative to the true value in the *detection* band f_D (left) and the forced band $f_{j,\text{ML}}$ (middle) along with the associated color $C = -2.5 \log(f_D/f_{j,\text{ML}})$ (right). The first and second-order analytic predictions from Appendix C and §6.1 are shown in red and blue, respectively. The estimate in the detection band f_D is biased high because the position parameters will move to better fit the noise in the data (see Figure 2). The estimate in the forced band $f_{j,\text{ML}}$ is biased low since the maximum-likelihood position in the detection band (x_D, y_D) is offset from the true position. The biases in the detection band and forced band compound when considering the color between the two bands. To leading order in the signal-to-noise ratio (SNR) in the *detection* band, the fractional flux bias in the forced band is $-\text{SNR}_D^{-2}$ and the bias in color is $-5/\ln 10 \times \text{SNR}_D^{-2}$.

The expectation value of $f_{j,\text{ML}}$ assuming (x_D, y_D) is fixed is

$$\mathbb{E}[f_{j,\text{ML}} | x_D, y_D] \approx f_j^* \times \frac{\sum_i p_i(x^*, y^*) p_i(x_D, y_D)}{\sum_i p_i^2(x_D, y_D)} \quad (63)$$

Since we expect the mismatched PSF term to be smaller than the matched PSF term $\sum_i p_i(x^*, y^*) p_i(x_D, y_D) \leq \sum_i p_i^2(x_D, y_D)$, this implies that $\mathbb{E}[f_{j,\text{ML}} | x_D, y_D] \leq f_j^*$ so that our ML flux densities are underestimated. Note that this bias tends to zero as $(x_{\text{ML}}, y_{\text{ML}}) \rightarrow (x^*, y^*)$, again confirming that our ML estimator is consistent in the limit of infinite SNR.

Subsequently taking the expectation value over position then gives the general expression

$$\mathbb{E}[f_{j,\text{ML}}] \approx f_j^* \times \iint \frac{\sum_i p_i(x^*, y^*) p_i(x_D, y_D)}{\sum_i p_i^2(x_D, y_D)} P(x_D, y_D | \theta^*, \mathbf{C}_\theta) dx_D dy_D \quad (64)$$

where $P(x_D, y_D | \theta^*, \mathbf{C}_\theta)$ is a 2-D multivariate normal distribution for (x, y) based on the FIM (§4). While this integral does not have an analytic solution, since we expect the bias to increase as (x_D, y_D) becomes progressively more offset from (x^*, y^*) , performing an average over possible ML positions further away from the true position should not be able to change our overall bias from an underestimate to an overestimate. Therefore, we arrive at the general conclusion that

$$\mathbb{E}[f_{j,\text{ML}}] \lesssim f_j^* \quad (65)$$

In other words, while our ML flux density estimates tend to be *overestimated* in the detection band, they will tend to be *underestimated* in all other bands. The severity of this (reverse) bias depends on the exact properties of the PSF in each band relative to the detection band (which establishes the ML position and associated covariances).

In the particular case where we have a circular Gaussian PSF with a standard deviation of s pixels, we can evaluate these biases explicitly. At a fixed offset $r_D^2 = (x_D - x^*)^2 + (y_D - y^*)^2$, the expected value of $f_{j,\text{ML}}$ is

$$\mathbb{E}[f_{j,\text{ML}} | r_D^2] = f_j^* \times \exp\left(\frac{-r_D^2}{4s^2}\right) \quad (66)$$

Assuming that the covariance between x_D and y_D is small such that we can approximate the errors as $\sigma_{D,x}^2 = \sigma_{D,y}^2$, the error-normalized offset will be distributed as

$$\frac{(x_D - x^*)^2}{\sigma_{D,x}^2} + \frac{(y_D - y^*)^2}{\sigma_{D,y}^2} = \frac{r_D^2}{\sigma_{D,x}^2} \sim \chi_2^2 \quad (67)$$

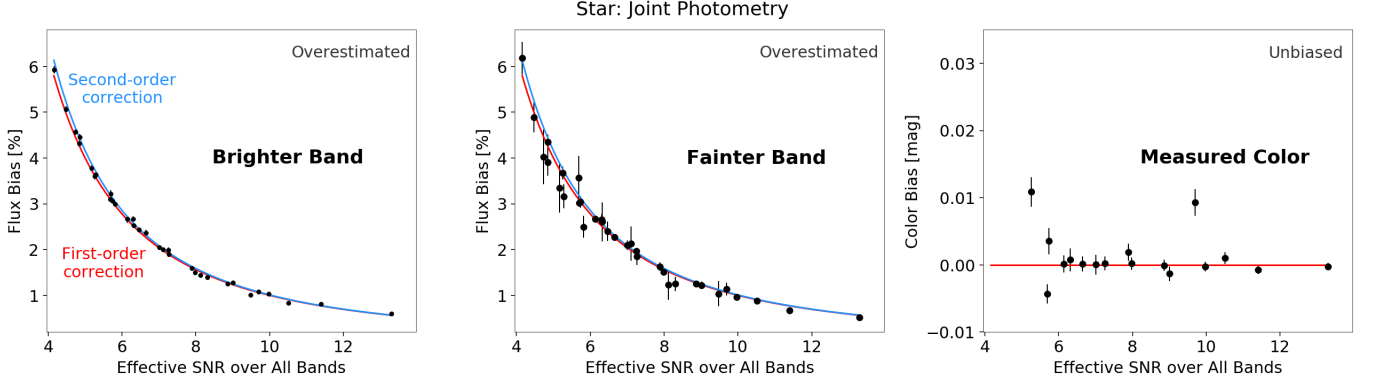


Figure 8. As Figure 7, but for simultaneous two-band photometry with a common (x, y) position. The position parameters move to better fit the noise in both bands, splitting the increase in the log-likelihood and estimated flux between both bands. If the two bands have the same PSF size, the fractional flux bias in both bands is determined by the combined SNR, regardless of color. Thus, the measured color is not affected by these flux biases, unlike the forced photometry case shown in Figure 7. To leading order in the combined signal-to-noise ratio (SNR), the fractional flux bias in both bands is $\text{SNR}_{\text{tot}}^{-2}$.

This implies that

$$r_D \sim \text{Rayleigh}(\sigma_{D,x}) \quad (68)$$

where $\text{Rayleigh}(\sigma_{D,x})$ is the Rayleigh distribution with scale parameter $\sigma_{D,x}$. Marginalizing over r_D then yields

$$\mathbb{E}[f_{j,\text{ML}}] = f_j^* \times \frac{2s^2}{2s^2 + \sigma_{D,x}^2} \quad (69)$$

Assuming a Gaussian PSF in the detection band with standard deviation s_D and $\sigma_{x,D}^2 = 8\pi s_D^4 \sigma_D^2 / f_D^2 \approx 2s_D^2 \sigma_{f,D}^2 / f_D^2$, we get

$$\mathbb{E}[f_{j,\text{ML}}] \approx f_j^* \left(1 + \frac{s_D^2 \sigma_{f,D}^2}{s^2 f_D^2} \right)^{-1} \quad (70)$$

This corresponds to a fractional bias of

$$\frac{\delta_{f_{j,\text{ML}}}}{f_{j,\text{ML}}} \equiv 1 - \frac{f_j^*}{\mathbb{E}[f_{j,\text{ML}}]} \approx -\frac{s_D^2 \sigma_{f,D}^2}{s^2 f_D^2} \quad (71)$$

In practice, we find that to properly model the bias at lower SNR requires incorporating a slightly higher-order Taylor expansion of our results (i.e. going from 2nd to 4th-order). As above, this expansion in general is non-trivial. However, it can be evaluated explicitly for circular Gaussian PSFs, as shown in Appendix G. Including this additional term then gives

$$\frac{f_j^*}{\mathbb{E}[f_{j,\text{ML}}]} - 1 \approx -\frac{s_D^2 \tilde{\sigma}_{f_D}^2}{s^2 f_D^{*2}} - \left[\frac{7s_D^2}{s^2} - \frac{s_D^4}{s^4} \right] \frac{\tilde{\sigma}_{f_D}^4}{f_D^{*4}} \quad (72)$$

We test our predictions for forced photometry by creating a set of simulated point-source images in two bands, running maximum-likelihood photometry on one band (the detection band) and forced photometry on the other (the forced band). Our simulated images have a point-source with a circular Gaussian PSF of $\sigma = 2$ pixels in the center of a 101×101 pixel image in each band with iid Gaussian noise in each pixel. We simulate sources with nine fluxes ranging from 4.0σ to 9.4σ in the detection band, evenly spaced in $1/\text{SNR}$. For each detection band flux, we consider four different forced band fluxes: $1\times$, $2\times$, $4\times$, and $8\times$ fainter than the flux in the detection band. For each flux combination, we create 100,000 different simulated images. Figure 7 shows that the flux in the detection band is overestimated and the flux in the forced band is underestimated, both by a fraction depending on the SNR in the detection band, as well as the bias on the measured color $C = -2.5 \log(f_D / f_{j,\text{ML}})$.

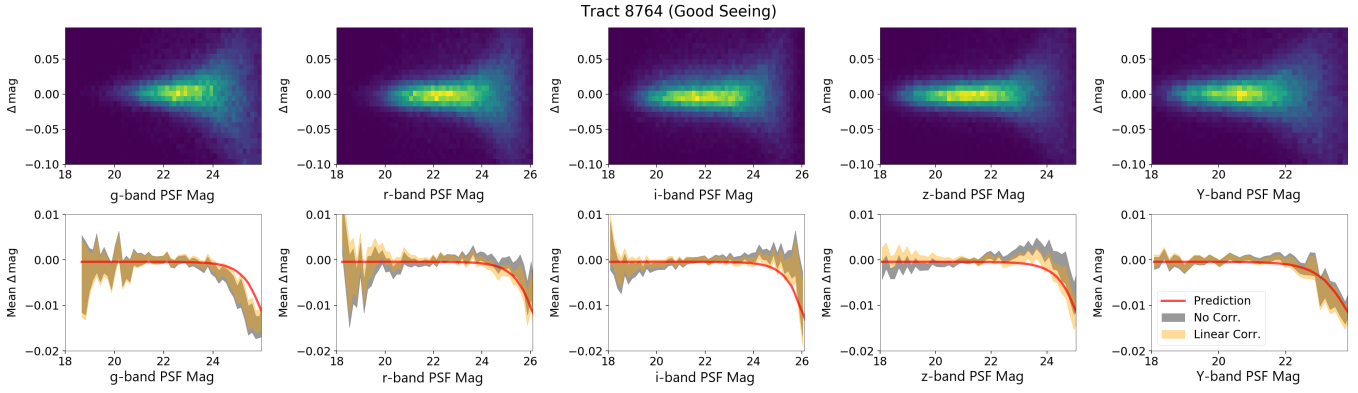


Figure 9. Top: The distribution of magnitude offsets in the *grizy* bands from HSC-SSP SynPipe artificial star tests as a function of input (true) magnitude for a tract with good seeing ($< 1''$). **Bottom:** The mean magnitude offsets as a function of magnitude from the top panel with (yellow) and without (gray) a simple linear correction to account for observed systematic trends. The mean predicted first-order analytic correction (SNR^{-2}) is shown in red. The mean magnitude offsets have been shifted to accommodate zero-point differences. Note the difference in scale between the top and bottom panels, highlighted the subtlety of the derived bias. Our analytic prediction provides a reasonable fit to the data, especially once the observed linear bias has been accounted for.

6.2. Unforced Photometry in All Bands

When the object is modeled simultaneously across bands (i.e. with a common (x, y) position), using Cochran's theorem reveals that the flux bias will be distributed between the bands but not how it is distributed. To calculate the bias in each band, we use the bias tensor formulation introduced by Cox & Snell (1968), which shows that the leading-order term in this bias for parameter s is

$$\delta_s(\boldsymbol{\theta}_{\text{ML}}) = \sum_{r,t,u} (\mathcal{F}^{-1}(\boldsymbol{\theta}_{\text{ML}}))_{rs} (\mathcal{F}^{-1}(\boldsymbol{\theta}_{\text{ML}}))_{tu} (\mathcal{B}(\boldsymbol{\theta}_{\text{ML}}))_{rtu} \quad (73)$$

where

$$(\mathcal{B}(\boldsymbol{\theta}_{\text{ML}}))_{rtu} \equiv \mathbb{E}_{\mathbf{D}} \left[\frac{1}{2} \partial_r \partial_t \partial_u \ln \mathcal{L}(\boldsymbol{\theta}_{\text{ML}}) + (\partial_t \ln \mathcal{L}(\boldsymbol{\theta}_{\text{ML}})) (\partial_r \partial_u \ln \mathcal{L}(\boldsymbol{\theta}_{\text{ML}})) \middle| \boldsymbol{\theta}_{\text{ML}} \right] \quad (74)$$

is the **bias tensor** and $\mathbb{E}_{\mathbf{D}}[\cdot | \boldsymbol{\theta}_{\text{ML}}]$ is the expectation value with respect to the data \mathbf{D} for $\boldsymbol{\theta}_{\text{ML}}$ fixed. This mirrors the FIM discussed in §4.

The derivation of the bias in f_{ML} with respect to f_{ML}^* using bias tensors in the single-band case is outlined in Appendix D. There, we show that

$$\delta_f(\boldsymbol{\theta}_{\text{ML}}) = \tilde{\sigma}_{f_{\text{ML}}}^2 \sum_{i \in \{x, y\}} \sigma_x^2 (\mathcal{B}(\boldsymbol{\theta}_{\text{ML}}))_{fii} \quad (75)$$

where

$$(\mathcal{B}(\boldsymbol{\theta}_{\text{ML}}))_{fxx} = (\mathcal{B}(\boldsymbol{\theta}_{\text{ML}}))_{fyy} = \frac{1}{2\sigma_x^2 f} \quad (76)$$

When using multiple bands, the bias for band i has the same terms as equation (75) for the single band case, but $\sigma_x^2 = (\mathcal{F}^{-1})_{xx}$ is smaller because all bands help constrain the position. However, in the bias tensor (equation 76), the σ_x^2 is the uncertainty in position that would have been obtained using only band i . If all bands have Gaussian PSFs with widths s_j , then the flux bias for band i is

$$\frac{\delta_{f_i}}{f_i} = \frac{\sigma_{f_i}^2}{f_i^2} \left(\sum_j \frac{f_j^2 s_i^2 \sigma_{f_i}^2}{f_i^2 s_j^2 \sigma_{f_j}^2} \right)^{-1} \quad (77)$$

where the sum over j is taken over all bands used in the fit. If all bands have the same PSF size s , then all bands have the same fractional flux bias of $(\sum_j \text{SNR}_j^2)^{-1}$.

We test our analytic predictions for simultaneous fitting by creating a set of two-band simulated point-source images with the same parameters as those used to make Figure 7 for forced photometry. Figure 8 shows that the fractional bias in both bands depends on the combined SNR, as predicted.

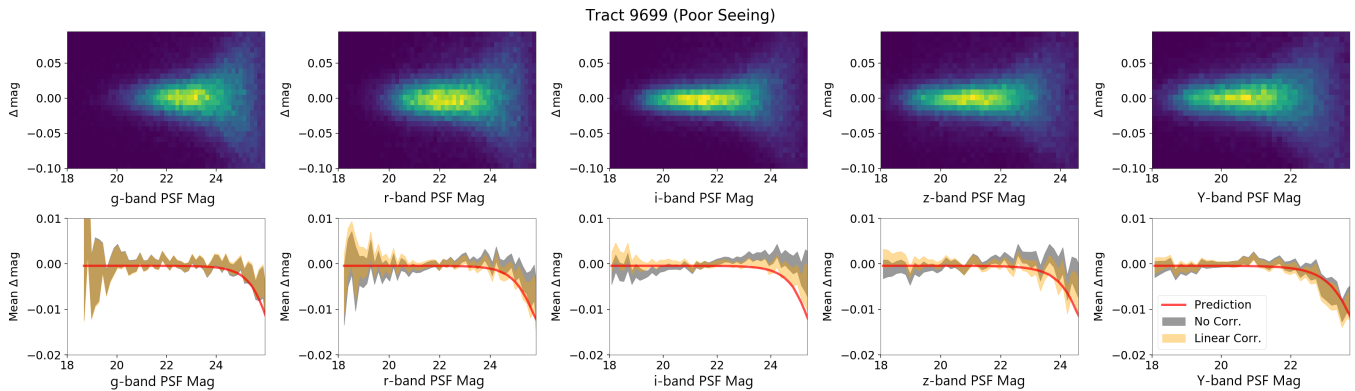


Figure 10. As Figure 9, but for a tract with poor seeing ($> 1''$). While a number of additional systematic trends remain present in the data, the analytic prediction continues to provide a good fit to the observed trends.

7. APPLICATION

While the results discussed in the previous sections are present in our simulations, we now turn our attention to real-world datasets to demonstrate that these effects are likely present in most datasets currently used in the astronomy community.

7.1. HSC SynPipe

We first investigate whether this effect is present in more realistic mock catalogs processed by real pipelines. In particular, we use simulated data from the Hyper Suprime Cam Subaru Strategic Program (HSC-SSP) Survey (Aihara et al. 2018) Synthetic Object Pipeline (SynPipe; Huang et al. 2018). In brief, SynPipe injects fake objects into real images which are then processed by the HSC-SSP Pipeline (Bosch et al. 2018) to test the accuracy/precision of various aspects of the pipeline. These objects are drawn from a realistic color and magnitude distribution based in part on data from the COSMOS survey, and so these mock tests represent fairly realistic realizations of the data seen by the HSC pipeline. See Huang et al. (2018) for additional details.

We analyze the PSF magnitudes for artificial star tests from two tracts (8764 and 9699) with good/poor seeing, respectively, processed using the same SynPipe configuration presented in Huang et al. (2018). The corresponding magnitude offsets and the predicted analytic relations are shown in Figures 9 and 10 for good seeing and poor seeing data, respectively. The magnitude offsets show good agreement with our model predictions, but include an additional systematic that is linear with magnitude. Investigating the source of this additional systematic is beyond the scope of this work.

One crucial aspect of these results is that the SynPipe tests nominally represent *forced* photometric extractions, with detection done in the *i* band. However, our results are almost entirely consistent with *unforced* photometry, where each band is derived separately. After some investigation, we find that this effect can be accounted for within the forced photometry algorithm used by the HSC pipeline, which effectively allows for limited “re-centering” in each band to improve the fit. Because the allowed range of positions is much larger than the relative positional uncertainties suggested by, e.g., σ_x (§2.2) in most cases, this process effectively undoes the forcing effect described in §6.1. This phenomenon – where “forced” photometry from a particular pipeline is not quite what its namesake suggests – highlights the importance of transparency when pipelines provide users with results for conducting detailed analysis.

7.2. Stripe 82

To show that this bias appears in real data, we also look at SDSS catalogs of Stripe 82 (Annis et al. 2014). Stars that are low signal-to-noise in individual “runs” should have magnitudes be biased high relative to their true values. While we do not have access to those true values, we approximate them using measurements taken from the combined images constructed from all the runs, which give much higher SNR measurements (with negligible bias) relative to the individual runs. We expect stars to be brighter, on average, in the individual run catalogs than in the stacked image catalog. Furthermore, each run and band will have a different bias, due to differences in seeing and sky brightness.

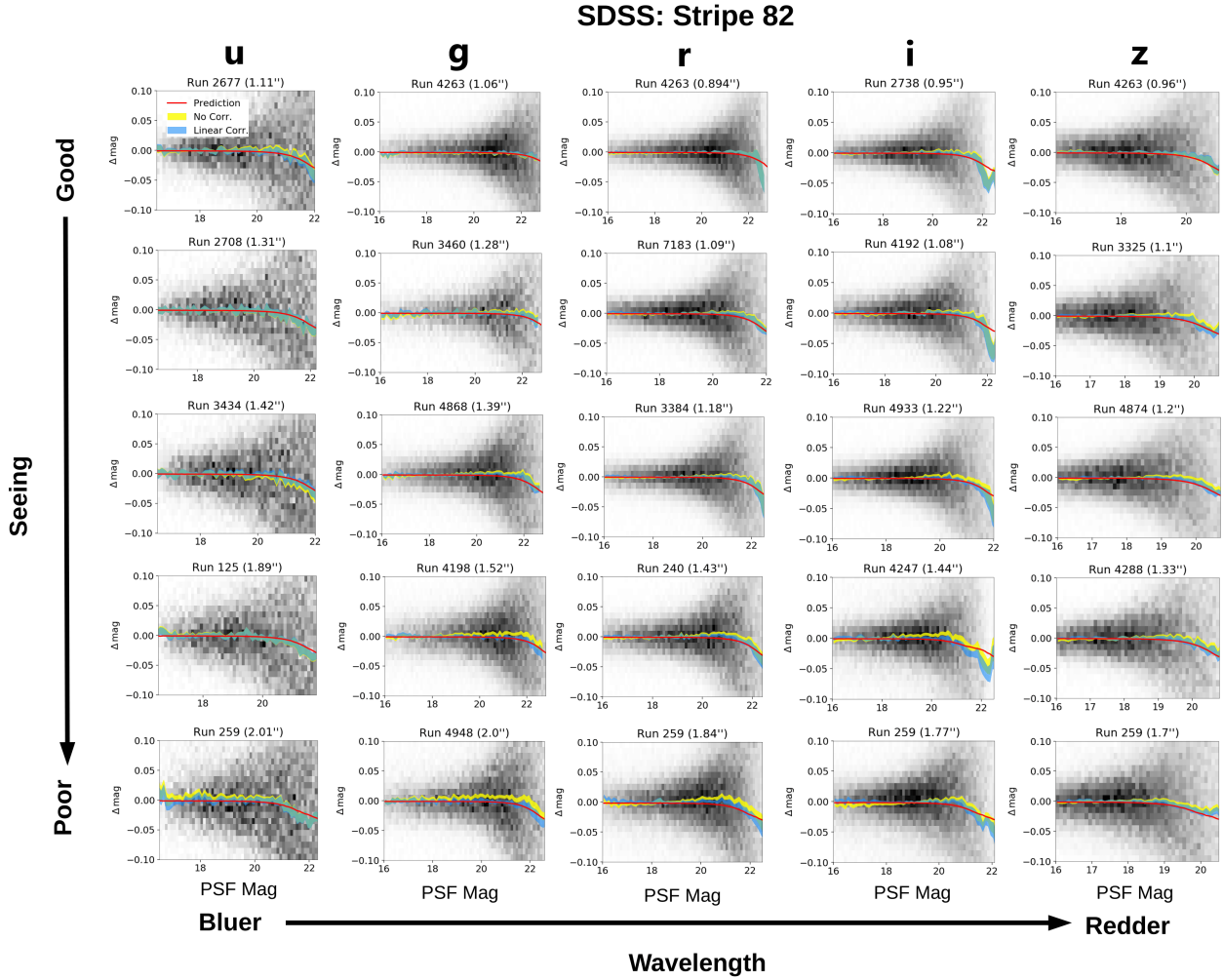


Figure 11. The distribution of PSF magnitude offsets in the *ugriz* bands for stars in SDSS Stripe 82 between individual runs and the measured values from the combined catalog. The general density is shown in grayscale, with the mean trends with and without a linear correction highlighted in blue and yellow, respectively, and our prediction (SNR^{-2}) in red. As Figure 9, the mean magnitude offsets have been shifted to accommodate additional systematic offsets. While a number of additional systematic trends similar to those seen in the HSC SynPipe data (Figures 9 and 10) are present, there is good agreement between the predicted and observed offsets.

Figure 11 shows the magnitude difference between the individual run catalogs and stacked image catalog for each band and over a range of seeing conditions. The faintest stars are biased brighter in the individual runs, in rough agreement with our predictions. It is interesting to note that the apparent systematic trends seen in these data mirror those in the HSC SynPipe tests, and that the photometry is also described as “forced” photometry from the SDSS pipeline. As the HSC pipeline is in part derived from the SDSS pipeline, these similarities bolster our suspicions that these results are most likely caused by the same algorithmic choices.

8. DISCUSSION

8.1. Aperture Photometry

We have shown that ML methods exhibit a generic bias when estimated the flux density of any particular isolated object from a given footprint. This bias becomes worse as the models become more complex (as is the case for

extended sources such as galaxies), and can behave in undesired ways when fitting across multiple bands (as with forced photometry).

Given these apparent drawbacks, some astronomers might wonder whether a return to aperture-based methods might present a compelling alternative. We want to offer a few arguments for why ML photometry should still be preferred and offer advice where aperture photometry might be more appropriate.

First, ML photometry performs better in the ideal case, where it is unbiased and follows the true error distribution, i.e. $f_{\text{ML}}^* \sim \mathcal{N}(f^*, \sigma_f^2)$. By contrast, an aperture will “miss” part of an object’s flux, leading to an *underestimate* in all cases. This correction is not expected to be the same for all sources unless the aperture is adaptively adjusted to match (a few times) the size of the PSF-convolved object, which is rarely the case. The “aperture corrections” involved to capture the total flux subsequently almost always serves as a dominant systematic hindering precise analyses.

Aperture photometry might also not eliminate the “centering bias” described in this work. Since an aperture also requires a position (x, y) to be centered on, determining a central position for the aperture will likely be subject to the same types of biases as the ML case (§3.2).¹² These expected centering offsets will result in variable amounts of flux being excluded from the aperture, likely biasing aperture photometry to a similar extent as ML photometry. Unlike in the ML case where these biases can be studied using statistical methods, however, apertures by nature make such studies much more difficult.

The derived errors from aperture photometry are also generally larger than those from ML photometry. In the ML case, we showed in §2 that the error for a point source is $\sigma_f^2 = A_{\text{psf}}\sigma^2$, where A_{psf} is the effective area of the PSF. For a Gaussian PSF with a standard deviation of s pixels, this gives $A_{\text{psf}}^G = \pi(2s)^2$. Since aperture photometry just sums all pixels within a given aperture, the equivalent error for an aperture with radius of $r = 2s$ pixels is just $\sigma_f^2 = \pi r^2 \sigma^2 = \pi(2s)^2 \sigma^2$. Any aperture larger than “2-sigma” then has errors that are strictly larger than those estimated from ML photometry, and even this $2s$ aperture excludes roughly 5% of the flux, requiring a significant aperture correction.

Aperture photometry is also inherently *unstable* as the aperture increases. While increasing the size of the aperture ensures a greater amount of the total flux is captured, it also increases the variance proportional to the size. While the SNR from ML photometry strictly *improves* as more data is added (see §3.2.1), the SNR from aperture photometry strictly *degrades* (ignoring aperture corrections).

Finally, aperture photometry is unable to integrate information across multiple bands/images. As discussed in §6.2, simultaneously fitting a single model across multiple images strictly improves the SNR and reduces the effective bias. Because apertures assume no model, they are unable to improve their SNR across multiple bands. While this comparison appears to be irrelevant in the examples shown in §7 which all exhibit tendencies equivalent to single-band unforced photometry, it will likely become more relevant in future survey pipelines.

Ultimately, aperture photometry is appealing because it is so simple: it assumes no model and is straightforward to apply to almost any isolated object. While this leads to many of the drawbacks mentioned above, it can also be desirable in cases where modeling complex sources can be difficult and/or the systematics involved limit the effective SNR of an object below that achievable with ML photometry. It thus serves a valuable purpose in cases where a model for the PSF and/or source cannot be cleanly determined *and* the source is relatively isolated; it should only be used judiciously in most other cases.

8.2. Stacked Catalogs

One direct corollary of our results is that users must be extremely careful what exactly “stacking” means when constructing catalogs and estimating photometry from sources. This is important because stacking can occur at multiple levels, ranging from the images themselves to the catalogs produced from them. In the former case, where images are combined *before* they are processed through a pipeline, modeling the results is somewhat equivalent to the simultaneous fitting approach discussed in §6.2. Assuming that each image has roughly the same error σ_f , the effective error from N images is expected to decrease to σ_f/\sqrt{N} and the bias to decrease accordingly. Stacking on the image level thus reduces both the error and the bias.

In the case where stacking is done on the *catalog* level, however, each observation will be biased, with a mean of $f_{\text{ML}} = f^*(1 + \text{SNR}^{-2})$ and error of σ_f . Averaging the results over many identical catalogs then will reduce the error to

¹² Indeed, apertures are often centered *using* positions determined from either model-fitting approaches or various simplistic heuristics (e.g., “peak hunting”).

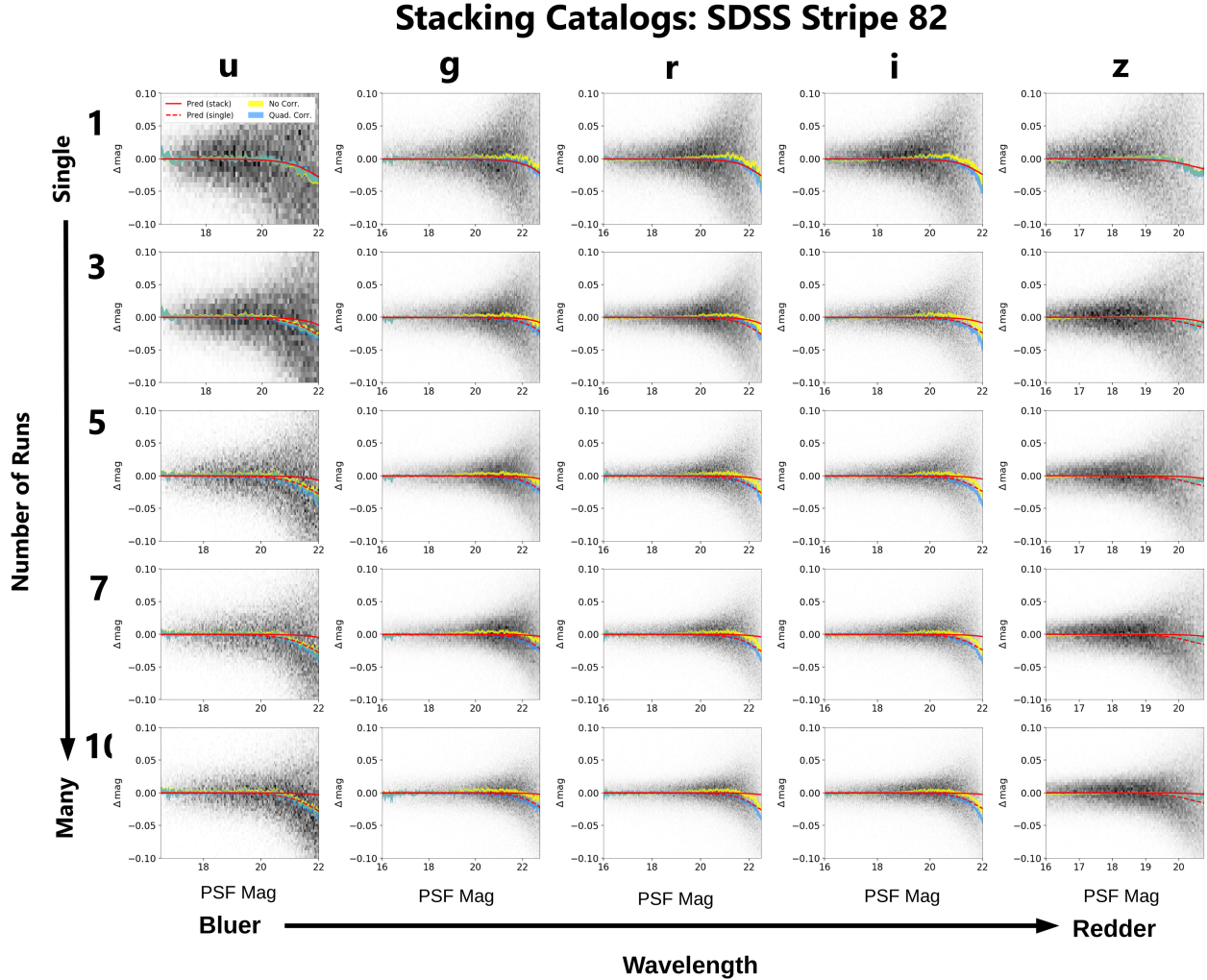


Figure 12. As Figure 11, but now for the case where we have constructed “deeper” catalogs by averaging objects detected in across individual runs *on the catalog level* rather than co-adding the images and we have applied a *quadratic* rather than linear correction for catalog-related biases. When dealing with a single run (top row), the predicted bias (which goes as SNR^{-2}) is a good fit to the data. Since this bias is the same across all runs, stacking observations on the catalog level (bottom rows) does not reduce this bias compared to the single-run case (red dashed lines) even though the nominal errors are smaller. Assuming that the bias decreases with the stack’s flux uncertainty leads to an underestimate of the bias (solid red lines), which can quickly become larger than the estimated errors. Stacking on the catalog-level can also compound other systematic effects introduced when modeling the images from each run.

σ_f/\sqrt{N} , but *will not* decrease the bias in any meaningful way. This implies that any measurement constructed from a stacked catalog may have systematic biases that far exceed the quoted statistical uncertainties.

Put another way, making catalogs from a series of images and then averaging the measurements across catalogs will not remove the flux density bias, because each catalog is individually biased. If inverse variance weighting is used and all images have the same PSF size, the fractional bias of the average will then be the reciprocal of the *average* SNR^2 . In contrast, the fractional bias from image stacking or simultaneous fitting is the reciprocal of the *total* SNR^2 , allowing multiple images of comparable SNR to drive down the bias. If catalogs are to be averaged, each catalog should first be *individually* debiased so that the average flux across catalogs is also unbiased. This procedure increases the variance in each catalog’s flux since the exact bias for each is not known (the bias-variance trade-off; see §3); however, this increase in variance is similar to that incurred by from debiasing the flux measured from a stacked image or simultaneous fit.

We illustrate this effect in Figure 12 by constructing “stacked catalogs”¹³ using the same SDSS Stripe 82 data used to generate Figure 11. As expected, the bias remains unchanged regardless of the number of runs used to generate the stack even as the estimated errors (and thus the bias we would *predict* from the stacked catalogs) decreases substantially.

8.3. Extension to Other Domains

While we have examined photometric biases in particular, this is by no means an exception to the fact that ML estimates can be routinely biased when dealing with particular parameters in a model. As such, users should consider carefully the *accuracy* (as opposed to the precision) demanded from ML parameter estimates. In cases where this is on the (sub-)percent-level, more robust approaches should be considered that can better model possible uncertainties.

As an example, spectral line measurements are likely to exhibit similar biases as photometry. As most algorithms to fit for emission and/or absorption features use ML methods as a function of 1-D position (in wavelength), we anticipate the amplitudes of spectral lines will be biased high, depending on the number of free parameters of the line profile. Line profile parameters may also be biased in a similar way to how the shape parameters of a galaxy are biased (§5.2). Using Cochran’s theorem, as in this paper (see Appendix C), leads to simple derivations of the bias for amplitude-like parameters that appear in the maximum likelihood, while the bias tensor formalism can be applied more generally. Whether or not this bias may be important depends both on the algorithms used to fit these lines and the particular science cases being considered.

9. CONCLUSION

In this paper, we study a photometric bias that arises from the maximum-likelihood (ML) estimator in model fitting photometry. It arises (in part) because the ML estimate can “soak up” a small amount of noise such that the fitted position is drawn away from the true position. This leads to an overestimate of the flux density, with a bias scaling with the inverse signal-to-noise ratio (SNR^{-2}) and the number of free parameters in the model. For example, it is 1% for a 10σ point-source and 2.5% for a 10σ 2-D Gaussian galaxy.

While this leads to an overestimate in the detection band, because the derived position is offset from the true position the flux density will be underestimated by the same SNR^{-2} in any other bands where the position is forced to the same value. This can double the effective bias in derived colors. By contrast, when all bands are modeled simultaneously, all bands are biased high, but less so than if they had been fit individually. In the case where all of the PSFs are the same size, this bias goes as $(\sum \text{SNR}^2)^{-1}$. If an object’s position is already known to great precision (for example, from a deeper or higher-resolution dataset), then forced photometry using this fixed position also does not suffer this bias. Methods that consider the distribution of possible positions, like Bayesian inference, do not exhibit this bias (see Appendix E).

We then show that this bias exists is likely common in many astronomical datasets using both mock HSC-like data and real SDSS data. The results further illustrate the importance of pipelines being transparent about the exact algorithmic implementation, since both tests are consistent with unforced photometry even though the data have been extracted using “forced” methods.

While we have examined photometric biases in particular, maximum likelihood estimates are biased in general. Spectral line measurements, for example, will exhibit similar biases as photometry, but in 1D (wavelength) instead of 2D (position). In cases where the accuracy of ML parameter estimates is required to be on the (sub-)percent-level, more robust approaches such as Markov Chain Monte Carlo should be considered.

Although maximum-likelihood estimators may be biased, we still strongly encourage using them over simpler aperture-based methods in most cases. While apertures are appealing because of their simplicity, they require difficult-to-model aperture corrections to account for missing flux and likely exhibit similar biases due to offsets in aperture centers relative to the true positions of objects. Apertures also cannot effectively incorporate information across multiple bands, which can substantially reduce any relevant biases by improving the effective signal-to-noise ratio.

Though we have shown derivations in a simplified case, with iid Gaussian noise, Gaussian PSFs, and Gaussian galaxy profiles, this bias is generic to maximum-likelihood photometry estimation and would still arise if these assumptions were relaxed. While calculating the relevant corrections will likely be more involved in more realistic cases, they are likely still tractable through the bias tensor formalism or through numerical simulations.

¹³ We “stack” our observations in flux density (linear) space to compute the weighted arithmetic mean. Note that stacking in magnitude (logarithmic) space (which computes the weighted geometric mean) introduces additional biases.

The authors would like to thank Jim Bosch, Charlie Conroy, Daniel Eisenstein, Song Huang, Željko Ivezić, Ben Johnson, Douglas Scott, Eddie Schlafly, Sandro Tacchella, and Catherine Zucker for discussion and feedback that helped to improve the quality of this work. JSS is eternally grateful to Rebecca Bleich for her patience and support.

JSS is supported by the National Science Foundation Graduate Research Fellowship Program. SKNP acknowledges support from the DIRAC Institute in the Department of Astronomy at the University of Washington. The DIRAC Institute is supported through generous gifts from the Charles and Lisa Simonyi Fund for Arts and Sciences, and the Washington Research Foundation.

The Hyper Suprime-Cam (HSC) collaboration includes the astronomical communities of Japan and Taiwan, and Princeton University. The HSC instrumentation and software were developed by National Astronomical Observatory of Japan (NAOJ), Kavli Institute for the Physics and Mathematics of the Universe (Kavli IPMU), University of Tokyo, High Energy Accelerator Research Organization (KEK) in Japan, Academia Sinica Institute for Astronomy and Astrophysics (ASIAA) in Taiwan, and Princeton University in the United States. Funding was contributed by the FIRST program from Japanese Cabinet Office; Ministry of Education, Culture, Sports, Science and Technology (MEXT); Japan Society for the Promotion of Science (JSPS); Japan Science and Technology Agency (JST); Toray Science Foundation; NAOJ; Kavli IPMU; KEK; ASIAA; and Princeton University.

This paper makes use of data products derived from software developed for the Large Synoptic Survey Telescope (LSST). We thank the LSST Project for making their code available as free software at <http://dm.lsstcorp.org>.

Funding for the Sloan Digital Sky Survey IV has been provided by the Alfred P. Sloan Foundation, the U.S. Department of Energy Office of Science, and the Participating Institutions. SDSS acknowledges support and resources from the Center for High-Performance Computing at the University of Utah. The SDSS web site is www.sdss.org.

SDSS is managed by the Astrophysical Research Consortium for the Participating Institutions of the SDSS Collaboration including the Brazilian Participation Group, the Carnegie Institution for Science, Carnegie Mellon University, the Chilean Participation Group, the French Participation Group, Harvard-Smithsonian Center for Astrophysics, Instituto de Astrofísica de Canarias, The Johns Hopkins University, Kavli Institute for the Physics and Mathematics of the Universe (IPMU) / University of Tokyo, the Korean Participation Group, Lawrence Berkeley National Laboratory, Leibniz Institut für Astrophysik Potsdam (AIP), Max-Planck-Institut für Astronomie (MPIA Heidelberg), Max-Planck-Institut für Astrophysik (MPA Garching), Max-Planck-Institut für Extraterrestrische Physik (MPE), National Astronomical Observatories of China, New Mexico State University, New York University, University of Notre Dame, Observatorio Nacional / MCTI, The Ohio State University, Pennsylvania State University, Shanghai Astronomical Observatory, United Kingdom Participation Group, Universidad Nacional Autónoma de México, University of Arizona, University of Colorado Boulder, University of Oxford, University of Portsmouth, University of Utah, University of Virginia, University of Washington, University of Wisconsin, Vanderbilt University, and Yale University.

REFERENCES

- Abazajian, K., Adelman-McCarthy, J. K., Agüeros, M. A., et al. 2004, *AJ*, 128, 502
- Aihara, H., Arimoto, N., Armstrong, R., et al. 2018, *PASJ*, 70, S4
- Annis, J., Soares-Santos, M., Strauss, M. A., et al. 2014, *ApJ*, 794, 120
- Bosch, J., Armstrong, R., Bickerton, S., et al. 2018, *PASJ*, 70, S5
- Brewer, B. J., Foreman-Mackey, D., & Hogg, D. W. 2013, *AJ*, 146, 7
- Condon, J. J. 1997, *Publications of the Astronomical Society of the Pacific*, 109, 166
- Cox, D. R., & Snell, E. J. 1968, *Journal of the Royal Statistical Society. Series B (Methodological)*, 30, 248. <http://www.jstor.org/stable/2984505>
- Gunn, J. E., Carr, M., Rockosi, C., et al. 1998, *The Astronomical Journal*, 116, 3040. <http://stacks.iop.org/1538-3881/116/i=6/a=3040>
- Huang, S., Leauthaud, A., Murata, R., et al. 2018, *Publications of the Astronomical Society of Japan*, 70, S6
- Iverson, R. J., Greve, T. R., Dunlop, J. S., et al. 2007, *MNRAS*, 380, 199
- King, I. R. 1983, *Publications of the Astronomical Society of the Pacific*, 95, 163
- Landolt, A. U. 1973, *AJ*, 78, 959
- . 1983, *AJ*, 88, 439
- . 1992, *AJ*, 104, 340
- LSST Science Collaboration, Abell, P. A., Allison, J., et al. 2009, *ArXiv e-prints*, arXiv:0912.0201
- Nyland, K., Lacy, M., Sajina, A., et al. 2017, *The Astrophysical Journal Supplement Series*, 230, 9

- Padmanabhan, N., Schlegel, D. J., Finkbeiner, D. P., et al. 2008, *ApJ*, 674, 1217
- Portillo, S. K. N., Lee, B. C. G., Daylan, T., & Finkbeiner, D. P. 2017, *AJ*, 154, 132
- Refregier, A., Kacprzak, T., Amara, A., Bridle, S., & Rowe, B. 2012, *MNRAS*, 425, 1951
- Schlafly, E. F., Meisner, A. M., & Green, G. M. 2019, arXiv e-prints, arXiv:1901.03337
- Stetson, P. B. 1987, *PASP*, 99, 191
- Turin, G. L. 1960, *IRE Trans. Information Theory*, 6, 311
- Wright, E. L., Eisenhardt, P. R. M., Mainzer, A. K., et al. 2010, *AJ*, 140, 1868

APPENDIX

A. RESULTS WITH CORRELATED NOISE

Assume the noise in our footprint to be Normally distributed such that

$$\hat{\mathbf{b}} \sim \mathcal{N}(\mathbf{b}^*, \mathbf{C}) \quad (\text{A1})$$

with mean vector \mathbf{b}^* and covariance matrix \mathbf{C} . The corresponding log-likelihood for a point source within our footprint is

$$\ln \mathcal{L}(x, y, f, \mathbf{b}) = -\frac{1}{2} \ln(\det(2\pi\mathbf{C})) - \frac{1}{2} (\hat{\mathbf{f}} - \mathbf{b} - f\mathbf{p}_{x,y})^T \mathbf{C}^{-1} (\hat{\mathbf{f}} - \mathbf{b} - f\mathbf{p}_{x,y}) \quad (\text{A2})$$

where \det is the determinant (i.e. the dimension-independent analog of area/volume).

A.1. Flux Density

At the ML flux $f_{\text{ML}}(x, y, \mathbf{b})$ the derivative with respect to f is zero such that

$$\partial_f \ln \mathcal{L}(x, y, f_{\text{ML}}, \mathbf{b}) = (\hat{\mathbf{f}} - \mathbf{b})^T \mathbf{C}^{-1} \mathbf{p}_{x,y} - f_{\text{ML}} \mathbf{p}_{x,y}^T \mathbf{C}^{-1} \mathbf{p}_{x,y} = 0 \quad (\text{A3})$$

which yields

$$f_{\text{ML}}(x, y, \mathbf{b}) = \frac{(\hat{\mathbf{f}} - \mathbf{b})^T \mathbf{C}^{-1} \mathbf{p}_{x,y}}{\mathbf{p}_{x,y}^T \mathbf{C}^{-1} \mathbf{p}_{x,y}} \quad (\text{A4})$$

The naive estimate (see §2.1) of the error/uncertainty $\tilde{\sigma}_f(x, y)$ is then

$$\tilde{\sigma}_f^2(x, y) = (\mathbf{p}_{x,y}^T \mathbf{C}^{-1} \mathbf{p}_{x,y})^{-1} \quad (\text{A5})$$

A.2. Position

The maximum-likelihood positions $(x_{\text{ML}}, y_{\text{ML}})$ can likewise be defined via

$$\partial_x \ln \mathcal{L}(x_{\text{ML}}, y, f, \mathbf{b}) = f \left((\hat{\mathbf{f}} - \mathbf{b}) - f\mathbf{p}_{x_{\text{ML}},y} \right)^T \mathbf{C}^{-1} \partial_x \mathbf{p}_{x_{\text{ML}},y} = 0 \quad (\text{A6})$$

with a naive error/uncertainty of

$$\begin{aligned} \tilde{\sigma}_x^2(x_{\text{ML}}, y, f, \mathbf{b}) &= \frac{1}{f^2} \left(\partial_x \mathbf{p}_{x_{\text{ML}},y}^T \mathbf{C}^{-1} \partial_x \mathbf{p}_{x_{\text{ML}},y} - \frac{1}{f} \left((\hat{\mathbf{f}} - \mathbf{b}) - f\mathbf{p}_{x_{\text{ML}},y} \right)^T \mathbf{C}^{-1} \partial_x^2 \mathbf{p}_{x_{\text{ML}},y} \right)^{-1} \\ &\approx \frac{1}{f^2} (\partial_x \mathbf{p}_{x_{\text{ML}},y}^T \mathbf{C}^{-1} \partial_x \mathbf{p}_{x_{\text{ML}},y})^{-1} \end{aligned} \quad (\text{A7})$$

A.3. Background

The maximum-likelihood background \mathbf{b}_{ML} can likewise be defined using

$$\partial_{\mathbf{b}} \ln \mathcal{L}(x, y, f, \mathbf{b}_{\text{ML}}) = \mathbf{C}^{-1} (\hat{\mathbf{f}} - f\mathbf{p}(x, y) - \mathbf{b}_{\text{ML}}) = 0 \quad (\text{A8})$$

which gives

$$\mathbf{b}_{\text{ML}}(x, y, f) = \hat{\mathbf{f}} - f\mathbf{p}_{x,y} \quad (\text{A9})$$

The associated naive errors then are

$$\tilde{\mathbf{C}}_{\mathbf{b}} = \mathbf{C} \quad (\text{A10})$$

This result shouldn't be entirely surprising. In §2.3, we noted that the maximum-likelihood background is just the mean residual between the model $f\mathbf{p}_{x,y}$ and the data $\hat{\mathbf{f}}$ in our given $n \times m$ footprint. In the iid case where we have assumed a fixed value b across the footprint, we therefore take the average over all the pixels. In the case where every pixel has a separate possible value $b_{\text{ML},i}$ for the background, however, this leads to averaging done on a per-pixel basis for \mathbf{b}_{ML} . Since always over-fits the data by construction, we also derive results for the more realistic case where $\mathbf{b}_{\beta} \equiv \mathbf{b}(\beta)$ is actually a function of a k nuisance parameters β across the footprint in Appendix B.

A.4. Bias

As in §3, we can rewrite our likelihood in terms of random variable notation such that

$$\hat{\mathbf{f}} = f^* \mathbf{p}(x^*, y^*) + \mathbf{b}^* + \mathbf{C}^{1/2} \mathbf{Z} \sim \mathcal{N}(f^* \mathbf{p}(x^*, y^*) + \mathbf{b}^*, \mathbf{C}) \quad (\text{A11})$$

where each $Z_i \sim \mathcal{N}(0, 1)$ is an iid random variable drawn from the standard Normal distribution and $\mathbf{C}^{1/2}$ is the (symmetric) square root of the covariance matrix. The likelihood at the true position (x^*, y^*) and background b^* then is

$$\ln \mathcal{L}(x^*, y^*, f, \mathbf{b}^*) = -\frac{1}{2} \ln(\det(2\pi\mathbf{C})) - \frac{1}{2} ((f^* - f) \mathbf{p}_{x^*, y^*} + \mathbf{C}^{1/2} \mathbf{Z})^T \mathbf{C}^{-1} ((f^* - f) \mathbf{p}_{x^*, y^*} + \mathbf{C}^{1/2} \mathbf{Z}) \quad (\text{A12})$$

This gives a ML flux density estimate of

$$f_{\text{ML}}(x^*, y^*, \mathbf{b}^*) = f^* + \frac{\mathbf{p}_{x^*, y^*}^T \mathbf{C}^{-1/2} \mathbf{Z}}{\mathbf{p}_{x^*, y^*}^T \mathbf{C}^{-1} \mathbf{p}_{x^*, y^*}} \quad (\text{A13})$$

Since

$$\frac{\mathbf{p}_{x^*, y^*}^T \mathbf{C}^{-1/2} \mathbf{Z}}{\mathbf{p}_{x^*, y^*}^T \mathbf{C}^{-1} \mathbf{p}_{x^*, y^*}} \sim \mathcal{N}\left(0, \frac{\mathbf{p}_{x^*, y^*}^T \mathbf{C}^{-1} \mathbf{p}_{x^*, y^*}}{(\mathbf{p}_{x^*, y^*}^T \mathbf{C}^{-1} \mathbf{p}_{x^*, y^*})^2} = \tilde{\sigma}_f^2(x^*, y^*)\right) \quad (\text{A14})$$

we then recover

$$\boxed{f_{\text{ML}}(x^*, y^*, b^*) \sim \mathcal{N}(f^*, \tilde{\sigma}_f^2(x^*, y^*))} \quad (\text{A15})$$

following §3.1.

B. ERRORS WITH GENERAL BACKGROUND MODELS

In §A.3, we showed that the maximum-likelihood (ML) solution for a background model \mathbf{b} across all nm pixels is

$$\mathbf{b}_{\text{ML}}(x, y, f) = \hat{\mathbf{f}} - f \mathbf{p}_{x, y} \quad (\text{B16})$$

which had an error estimate of

$$\tilde{\mathbf{C}}_{\mathbf{b}} = \mathbf{C} \quad (\text{B17})$$

This result is singularly uninformative, because it implies that the “best” background model is exactly equal to the model residuals across the entire image.

In most cases, we often seek to parameterize the background as a smooth function $\mathbf{b}_{\beta} \equiv \mathbf{b}(\boldsymbol{\beta})$ of k nuisance parameters $\boldsymbol{\beta}$ across the footprint. This gives us

$$\partial_{\beta_i} \ln \mathcal{L}(x, y, f, \boldsymbol{\beta}_{\text{ML}}) = \partial_{\beta_i} \mathbf{b}_{\boldsymbol{\beta}_{\text{ML}}}^T \mathbf{C}^{-1} (\hat{\mathbf{f}} - f \mathbf{p}_{x, y} - \mathbf{b}_{\boldsymbol{\beta}_{\text{ML}}}) = 0 \quad (\text{B18})$$

which we can use to solve for $\boldsymbol{\beta}_{\text{ML}}$. Following §4, the error estimates can be derived by inverting the Fisher Information Matrix (FIM) whose elements are

$$(\mathcal{F}_{\boldsymbol{\beta}})_{ij}(x, y, f, \boldsymbol{\beta}_{\text{ML}}) = \partial_{\beta_i} \mathbf{b}_{\boldsymbol{\beta}_{\text{ML}}}^T \mathbf{C}^{-1} \partial_{\beta_j} \mathbf{b}_{\boldsymbol{\beta}_{\text{ML}}} - \partial_{\beta_i} \partial_{\beta_j} \mathbf{b}_{\boldsymbol{\beta}_{\text{ML}}}^T \mathbf{C}^{-1} (\hat{\mathbf{f}} - f \mathbf{p}_{x, y} - \mathbf{b}_{\boldsymbol{\beta}_{\text{ML}}}) \quad (\text{B19})$$

As before, if we assume that our overall residuals $\hat{\mathbf{f}} - f \mathbf{p}_{x, y} - \mathbf{b}_{\boldsymbol{\beta}_{\text{ML}}}$ are small and that our background model varies sufficiently slowly with respect to $\boldsymbol{\beta}$, we can approximate this as

$$\boxed{\mathcal{F}_{\boldsymbol{\beta}}(\boldsymbol{\beta}_{\text{ML}}) \approx \partial_{\boldsymbol{\beta}} \mathbf{b}_{\boldsymbol{\beta}_{\text{ML}}}^T \mathbf{C}^{-1} \partial_{\boldsymbol{\beta}} \mathbf{b}_{\boldsymbol{\beta}_{\text{ML}}}} \quad (\text{B20})$$

where $\partial_{\boldsymbol{\beta}} \mathbf{b}_{\boldsymbol{\beta}_{\text{ML}}}$ is the $nm \times k$ Jacobian. This implies that we can use the Jacobian to linearly project from the nm -dimensional “data space” into the k -dimensional parameter space.

C. MAXIMUM-LIKELIHOOD BIASES USING COCHRAN'S THEOREM

As discussed in §3.2, given the true values $(x^*, y^*, f^*, \mathbf{b}^*)$ of the position, flux density, and background, respectively, we can rewrite the likelihood of the noisy data as

$$\ln \mathcal{L}(x^*, y^*, f^*, \mathbf{b}^*) = -\frac{1}{2} \ln(\det(2\pi\mathbf{C})) - \frac{1}{2} \sum_i Z_i^2 \quad (\text{C21})$$

where $Z_1, \dots, Z_i \sim \mathcal{N}(0, 1)$ are again iid normal random variables and

$$\sum_{i=1}^{nm} Z_i^2 \sim \chi_A^2 \quad (\text{C22})$$

follows a chi-square distribution with $A = nm$ degrees of freedom. Assuming that the data are normally distributed and our ML parameters are also approximately Normally distributed, we can apply Cochran's theorem to get

$$(\hat{\mathbf{f}} - \mathbf{f}_{\theta_{\text{ML}}})^T \mathbf{C}^{-1} (\hat{\mathbf{f}} - \mathbf{f}_{\theta_{\text{ML}}}) \sim \chi_{A-p}^2 \quad (\text{C23})$$

Assuming the background is known (see §3.2.2), we note that we can relate the distribution of the sum of error normalized residuals around $f_{\text{ML}} \equiv f_{\text{ML}}(x_{\text{ML}}, y_{\text{ML}})$ in the decoupled-background case to those around $f_{\text{ML}}^* \equiv f_{\text{ML}}(x^*, y^*)$ for a constant background model b via

$$(\hat{\mathbf{f}} - f_{\text{ML}} \mathbf{p}_{x_{\text{ML}}, y_{\text{ML}}})^T \mathbf{C}^{-1} (\hat{\mathbf{f}} - f_{\text{ML}} \mathbf{p}_{x_{\text{ML}}, y_{\text{ML}}}) + X_2^2 \sim (\hat{\mathbf{f}} - f_{\text{ML}}^* \mathbf{p}_{x^*, y^*})^T \mathbf{C}^{-1} (\hat{\mathbf{f}} - f_{\text{ML}}^* \mathbf{p}_{x^*, y^*})$$

where $X_2^2 \sim \chi_2^2$ incorporates the noise “absorbed” by $(x_{\text{ML}}, y_{\text{ML}})$ and we have exploited the fact that $X_2^2 + X_{nm-2}^2 \sim \chi_{nm}^2$. Exploiting the fact that

$$\ln \mathcal{L}(x, y, f_{\text{ML}}) = \frac{f_{\text{ML}}^2(x, y)}{2\tilde{\sigma}_f^2(x, y)} \quad (\text{C24})$$

then allows us to rewrite the above result as

$$\hat{\mathbf{f}}^T \mathbf{C}^{-1} \hat{\mathbf{f}} - 2f_{\text{ML}} \hat{\mathbf{f}}^T \mathbf{C}^{-1} \mathbf{p}_{x_{\text{ML}}, y_{\text{ML}}} + \frac{f_{\text{ML}}^2}{\tilde{\sigma}_{f_{\text{ML}}}^2} + X_2^2 \sim \hat{\mathbf{f}}^T \mathbf{C}^{-1} \hat{\mathbf{f}} - 2f_{\text{ML}}^* \hat{\mathbf{f}}^T \mathbf{C}^{-1} \mathbf{p}_{x^*, y^*} + \frac{f_{\text{ML}}^{*,2}}{\tilde{\sigma}_{f_{\text{ML}}^*}^2} \quad (\text{C25})$$

Although the true position is not known, in the interest of deriving the impact on the flux we can take the approximation that $(x^*, y^*) \approx (x_{\text{ML}}, y_{\text{ML}})$, etc. for all terms that don't explicitly involve the flux density f . This leaves us with an equation of the form

$$c_1 f_{\text{ML}}^2 - 2c_2 f_{\text{ML}} + X_2^2 \sim c_1 (f_{\text{ML}}^*)^2 - 2c_2 f_{\text{ML}}^* \quad (\text{C26})$$

where $c_1 = \tilde{\sigma}_{f_{\text{ML}}}^{-2}$ and $c_2 = \hat{\mathbf{f}}^T \mathbf{C}^{-1} \mathbf{p}_{x_{\text{ML}}, y_{\text{ML}}}$ are roughly constant. This has a positive solution at

$$f_{\text{ML}}^* \sim \frac{c_2 + \sqrt{c_1^2 f_{\text{ML}}^2 - c_1 X_2^2 - 2c_1 c_2 f_{\text{ML}} + c_2^2}}{c_1} = \frac{c_2}{c_1} + f_{\text{ML}} \sqrt{1 - \frac{2c_2}{c_1 f_{\text{ML}}} - \frac{X_2^2}{c_1 f_{\text{ML}}^2} + \frac{c_2^2}{c_1^2 f_{\text{ML}}^2}} \quad (\text{C27})$$

Since c_1 and c_2 are known for a given $(x_{\text{ML}}, y_{\text{ML}})$ and the distribution of $X_2^2 \sim \chi_2^2$ is known exactly, this gives an expression for the distribution of the unbiased ML estimator f_{ML}^* . In general, assuming that the residuals are sufficiently small such that $c_2 \approx 0$, this reduces to

$$f_{\text{ML}}^* \sim f_{\text{ML}} \sqrt{1 - X_2^2 \frac{\tilde{\sigma}_{f_{\text{ML}}}^2}{f_{\text{ML}}^2}} \quad (\text{C28})$$

This can be immediately generalized to a model with p model parameters θ (excluding the background b) to get

$$f_{\text{ML}}^* \sim f_{\text{ML}} \sqrt{1 - X_{p-1}^2 \frac{\tilde{\sigma}_{f_{\text{ML}}}^2}{f_{\text{ML}}^2}} \quad (\text{C29})$$

We can write this in a slightly more intuitive form by Taylor expanding around small $\tilde{\sigma}_{f_{\text{ML}}}/f_{\text{ML}}$ to get

$$f_{\text{ML}}^* \approx f_{\text{ML}} \left[1 - \frac{X_{p-1}^2}{2} \frac{\tilde{\sigma}_{f_{\text{ML}}}^2}{f_{\text{ML}}^2} \right] \quad (\text{C30})$$

This gives a fractional bias of

$$1 - \frac{\mathbb{E}[f_{\text{ML}}^*]}{f_{\text{ML}}} \equiv \frac{\delta_{f_{\text{ML}}}}{f_{\text{ML}}} \approx \frac{p-1}{2} \frac{\tilde{\sigma}_{f_{\text{ML}}}^2}{f_{\text{ML}}^2}, \quad \frac{\mathbb{V}[f_{\text{ML}}^*]}{\tilde{\sigma}_{f_{\text{ML}}}^2} \approx \frac{p^2 - 4p + 7}{4} \frac{\sigma_{f_{\text{ML}}}^2}{f_{\text{ML}}^2} \quad (\text{C31})$$

At lower SNR it is necessary to include the second-order term $\frac{X_{p-1}^4}{8} \frac{\sigma_{f_{\text{ML}}}^4}{f_{\text{ML}}^4}$ from the Taylor expansion to properly model behavior. Including this term gives a modified fractional bias of

$$\frac{\delta_{f_{\text{ML}}}}{f_{\text{ML}}} \approx \frac{p-1}{2} \frac{\tilde{\sigma}_{f_{\text{ML}}}^2}{f_{\text{ML}}^2} + \frac{p^2 - 1}{8} \frac{\tilde{\sigma}_{f_{\text{ML}}}^4}{f_{\text{ML}}^4} \quad (\text{C32})$$

For a typical point source model with $p = 3$ parameters (x, y, f) , this becomes

$$\frac{\delta_{f_{\text{ML}}}}{f_{\text{ML}}} \approx \frac{\tilde{\sigma}_{f_{\text{ML}}}^2}{f_{\text{ML}}^2} + \frac{\tilde{\sigma}_{f_{\text{ML}}}^4}{f_{\text{ML}}^4} \quad (\text{C33})$$

D. MAXIMUM-LIKELIHOOD BIASES USING BIAS TENSORS

As discussed in §5, ML estimators have a bias δ which tends to zero as the signal-to-noise ratio (SNR) increases. Cox & Snell (1968) found that the leading-order bias term for any parameter s can be found with

$$\delta_s(\boldsymbol{\theta}_{\text{ML}}) = \sum_{r,t,u} (\mathcal{F}^{-1}(\boldsymbol{\theta}_{\text{ML}}))_{rs} (\mathcal{F}^{-1}(\boldsymbol{\theta}_{\text{ML}}))_{tu} (\mathcal{B}(\boldsymbol{\theta}_{\text{ML}}))_{rtu} \quad (\text{D34})$$

where

$$(\mathcal{B}(\boldsymbol{\theta}_{\text{ML}}))_{rtu} \equiv \mathbb{E}_{\mathbf{D}} \left[\frac{1}{2} \partial_r \partial_t \partial_u \ln \mathcal{L}(\boldsymbol{\theta}_{\text{ML}}) + (\partial_t \ln \mathcal{L}(\boldsymbol{\theta}_{\text{ML}})) (\partial_r \partial_u \ln \mathcal{L}(\boldsymbol{\theta}_{\text{ML}})) \middle| \boldsymbol{\theta}_{\text{ML}} \right] \quad (\text{D35})$$

is the bias tensor and $\mathbb{E}_{\mathbf{D}}[\cdot | \boldsymbol{\theta}_{\text{ML}}]$ is the expectation value with respect to the data \mathbf{D} for $\boldsymbol{\theta}_{\text{ML}}$ fixed.

With the background $b = b^*$ fixed, the non-zero terms in the flux density bias δ_f are

$$\delta_f(\boldsymbol{\theta}_{\text{ML}}) = \tilde{\sigma}_{f_{\text{ML}}}^2 \sum_{i \in \{x, y\}} \sigma_x^2 (\mathcal{B}(\boldsymbol{\theta}_{\text{ML}}))_{fii} \quad (\text{D36})$$

since the off-diagonal elements of the FIM with respect to position (x, y) are zero (§4.3) and we have substituted in for $(\mathcal{F}^{-1}(\boldsymbol{\theta}_{\text{ML}}))_{ff} = \tilde{\sigma}_{f_{\text{ML}}}^2$ and $(\mathcal{F}^{-1}(\boldsymbol{\theta}_{\text{ML}}))_{xx} = (\mathcal{F}^{-1}(\boldsymbol{\theta}_{\text{ML}}))_{yy} = \sigma_x^2$. Under similar assumptions as §3.2, is it straightforward to show that

$$(\mathcal{B}(\boldsymbol{\theta}_{\text{ML}}))_{fxx} = (\mathcal{B}(\boldsymbol{\theta}_{\text{ML}}))_{fyy} = \frac{1}{2\sigma_x^2 f} \quad (\text{D37})$$

and thus:

$$\delta_{f_{\text{ML}}} = \frac{\tilde{\sigma}_{f_{\text{ML}}}^2}{f_{\text{ML}}}. \quad (\text{D38})$$

Substituting in for the definition of δ_f allows us to rewrite this as

$$\mathbb{E}[f_{\text{ML}}^*] = f_{\text{ML}} \left(1 - \frac{\tilde{\sigma}_{f_{\text{ML}}}^2}{f_{\text{ML}}^2} \right) \quad (\text{D39})$$

which reproduces equation (28).

With the background b free, the flux bias has the same terms as Equation D36 except that $(\mathcal{F}^{-1}(\boldsymbol{\theta}_{\text{ML}}))_{ff} = \sigma_{f_{\text{ML}}}^2 \geq \tilde{\sigma}_{f_{\text{ML}}}^2$ due to the covariance between the flux and background. Solving and rearranging as above then gives

$$\mathbb{E}[f_{\text{ML}}^*] = f_{\text{ML}} \left(1 - \frac{\sigma_{f_{\text{ML}}}^2}{f_{\text{ML}}^2} \right) \quad (\text{D40})$$

which reproduces equation (35).

E. UNBIASEDNESS OF MARGINALIZED MEAN FLUX

While the ML solution is the mode of the likelihood distribution, the *mean* flux density f_{mean} , marginalizing over position (x, y) , need not be the ML flux density f_{ML} . Here, we show that the posterior mean flux is unbiased to order SNR^{-2} in a specific case (flat priors and Gaussian PSF) for illustrative purposes.

As discussed in §2, the maximum likelihood flux $f_{\text{ML}}(x, y)$ varies with position and is maximized at $(x_{\text{ML}}, y_{\text{ML}})$ assuming the background b is known. While first derivative of $f_{\text{ML}} \equiv f_{\text{ML}}(x_{\text{ML}}, y_{\text{ML}})$ with position is zero (by definition), the second derivative is

$$\partial_x^2 f_{\text{ML}} \approx \frac{1}{\sum_j p_j^2} \sum_i \partial_x^2 p_i \hat{f}_i \quad (\text{E41})$$

under the same oversampled/smoothness assumptions discussed in §2.2. For a circular Gaussian PSF with standard deviation of s pixels, the second derivative of the PSF is

$$\partial_x^2 p_i = \frac{\Delta x_i^2 - s^2}{s^4} p_i \quad (\text{E42})$$

where Δx_i is the difference in the x-coordinate of the center of pixel i and the source. Taking

$$\frac{\sum_i \Delta x_i^2 p_i^2}{\sum_j p_j^2} \approx \frac{s^2}{2} \quad (\text{E43})$$

and approximating the counts around the source as $\hat{f}_i \approx f_{\text{ML}} p_i$ then gives

$$\partial_x^2 f_{\text{ML}} \approx -\frac{f_{\text{ML}}}{2s^2}. \quad (\text{E44})$$

using the definition of f_{ML} from equation (7).

Near the ML position, the ML flux density is approximately

$$f_{\text{ML}}(x, y) \approx f_{\text{ML}} \left[1 - \frac{(x - x_{\text{ML}})^2 + (y - y_{\text{ML}})^2}{4s^2} \right] \quad (\text{E45})$$

The likelihood can then be approximated (up to a constant factor Z) as

$$\mathcal{L}(x, y, f) = Z \exp \left(-\frac{(x - x_{\text{ML}})^2 + (y - y_{\text{ML}})^2}{2\sigma_x^2(f_{\text{ML}})} - \frac{(f - f_{\text{ML}}(x, y))^2}{2\sigma_f^2(f_{\text{ML}})} \right) \quad (\text{E46})$$

where we have taken $\tilde{\sigma}_x^2 = \tilde{\sigma}_y^2$ since our PSF is circular. The mean flux density f_{mean} after marginalizing over position is defined as

$$f_{\text{mean}} \equiv \frac{\iiint \mathcal{L}(x, y, f) f \, df \, dx \, dy}{\iiint \mathcal{L}(x, y, f) \, df \, dx \, dy} \quad (\text{E47})$$

Integrating over the flux density f yields

$$f_{\text{mean}} \approx \frac{\iint f_{\text{ML}}(x, y) \exp \left(-\frac{(x - x_{\text{ML}})^2 + (y - y_{\text{ML}})^2}{2\sigma_x^2(f_{\text{ML}})} \right) \, dx \, dy}{\iint \exp \left(-\frac{(x - x_{\text{ML}})^2 + (y - y_{\text{ML}})^2}{2\sigma_x^2(f_{\text{ML}})} \right) \, dx \, dy} \quad (\text{E48})$$

and then using equation (E45) for $f_{\text{ML}}(x, y)$ gives

$$f_{\text{mean}} \approx f_{\text{ML}} \left(1 - \frac{\sigma_x^2(f_{\text{ML}})}{2s^2} \right) \quad (\text{E49})$$

Substituting in $\sigma_x^2(f) = 2\sigma_f^2 s^2 / f^2$ for our circular Gaussian PSF then gives

$$f_{\text{mean}} \approx f_{\text{ML}} \left(1 - \frac{\sigma_{f_{\text{ML}}}^2}{f_{\text{ML}}^2} \right) = \mathbb{E}[f_{\text{ML}}^*] \quad (\text{E50})$$

where $\sigma_{f_{\text{ML}}} \equiv \sigma_f(f_{\text{ML}})$ and $f_{\text{ML}}^* = f_{\text{ML}}(x^*, y^*)$ are defined as in §3.

Since we showed §3 that the ML estimator at the true position f_{ML}^* is unbiased, this explicitly demonstrates that the mean flux density, marginalized over position, is also unbiased.

F. ADDITIONAL ERRORS IN GAUSSIAN MODEL

For an object described by a Gaussian with free shape parameters, the covariances between the flux density and shape parameters increases the error in flux density. To find these covariances, we need second partial derivatives of the log-likelihood

$$\partial_{\alpha\beta} \ln \mathcal{L} = \frac{1}{\sigma^2} \sum_i (\hat{f}_i - fp_i(x, y) - b) \partial_{\alpha\beta} (fp_i(x, y) + b) - \partial_{\alpha} (fp_i(x, y) + b) \partial_{\beta} (fp_i(x, y) + b) \quad (\text{F51})$$

with p_i being the galaxy model convolved with the PSF and α, β indexing the parameters of the galaxy. To fill in the FIM, we take the expectation value of the second derivatives with the parameters fixed to their true values. The residuals about the true parameters $\hat{f}_i - fp_i$ are zero in expectation, so

$$\mathcal{F}_{\alpha\beta} = \frac{1}{\sigma^2} \sum_i \partial_{\alpha} (fp_i(x, y) + b) \partial_{\beta} (fp_i(x, y) + b) \approx \iint \partial_{\alpha} (fp(x, y) + b) \partial_{\beta} (fp(x, y) + b) dx dy \quad (\text{F52})$$

in the well-sampled limit, with

$$p(x, y) = \frac{1}{2\pi a_1 a_2} \exp\left(-\frac{(x \cos \varphi + y \sin \varphi)^2}{2a_1^2} - \frac{(-x \sin \varphi + y \cos \varphi)^2}{2a_2^2}\right) \quad (\text{F53})$$

Many of the off-diagonal elements are zero due to the symmetries of $p(x, y)$, so the FIM is diagonal except for the entries involving f , b , a_1 , and a_2 . The FIM for these four parameters is

$$\mathcal{F} = \frac{1}{\sigma^2} \begin{bmatrix} \frac{1}{4\pi a_1 a_2} & 1 & -\frac{f}{8\pi a_1^2 a_2} & -\frac{f}{8\pi a_1 a_2^2} \\ 1 & A & 0 & 0 \\ -\frac{f}{8\pi a_1^2 a_2} & 0 & \frac{3f^2}{16\pi a_1^3 a_2} & \frac{f^2}{16\pi a_1^2 a_2^2} \\ -\frac{f}{8\pi a_1 a_2^2} & 0 & \frac{f^2}{16\pi a_1^2 a_2^2} & \frac{3f^2}{16\pi a_1 a_2^3} \end{bmatrix} \quad (\text{F54})$$

Note that $\mathcal{F}_{ff} = (A_{\text{psf}} \sigma^2)^{-1}$ for a galaxy and so without accounting for the covariances, $\tilde{\sigma}_f^2 = A_{\text{psf}} \sigma^2$. Taking the covariances into account by inverting the FIM yields:

$$(\mathcal{F}^{-1})_{ff} = \frac{8\pi a_1 a_2 \sigma^2}{1 - 8\pi a_1 a_2 / A} = \frac{2A_{\text{psf}} \sigma^2}{1 - 2A_{\text{psf}} / A} \quad (\text{F55})$$

G. SECOND-ORDER EXPANSION IN FLUX DENSITY

As discussed in Section §6.1, fixing the position of an object to the best-fit from a detection band D leads to an underestimate in the flux density in all other bands. If the detected position is distributed as a 2-D Gaussian of width σ_x about the true position, the average best-fit flux is given by Equation 69:

$$\mathbb{E}[f_{j,\text{ML}}] = f_j^* \times \frac{2s^2}{2s^2 + \sigma_{D,x}^2} \quad (\text{G56})$$

At low signal to noise, the position error obtained by inverting the second derivative with respect to position (Equation 14) needs to be corrected by higher-order terms. The maximum-likelihood is found by setting the partial derivatives of the log-likelihood to zero. We Taylor expand the partial derivatives to leading order about the true parameters (x^*, y^*, f^*) :

$$0 = \partial_{\alpha} \ln \mathcal{L}(x_{\text{ML}}, y_{\text{ML}}, f_{\text{ML}}) \approx \partial_{\alpha} \ln \mathcal{L}(x^*, y^*, f^*) + \sum_{\beta} (\beta_{\text{ML}} - \beta^*) \partial_{\alpha\beta}^2 \ln \mathcal{L}(x^*, y^*, f^*) \quad (\text{G57})$$

with $\alpha, \beta \in \{x, y, f\}$. Evaluating the partial derivatives at the true parameters yields

$$\partial_{\alpha} \ln \mathcal{L}(x^*, y^*, f^*) = \frac{1}{\sigma^2} \sum_i \sigma Z_i \partial_{\alpha} (fp_i(x, y))|_{\theta=\theta^*} \quad (\text{G58})$$

$$\partial_{\alpha\beta} \ln \mathcal{L}(x^*, y^*, f^*) = \frac{1}{\sigma^2} \sum_i \sigma Z_i \partial_{\alpha\beta} (fp_i(x, y))|_{\theta=\theta^*} - \partial_{\alpha} (fp_i(x, y))|_{\theta=\theta^*} \partial_{\beta} (fp_i(x, y))|_{\theta=\theta^*} \quad (\text{G59})$$

with $Z_i = (\hat{f}_i - f^* p_i(x^*, y^*))$ being independent, normally distributed variables with mean zero and unit variance. The sum over pixels of the second term of Equation G59 can be approximated in the oversampled limit with integrals over the PSF and its derivatives. Using Equations G58 and G59, Equation G57 can be written as a matrix equation:

$$0 = \sigma \begin{bmatrix} \zeta \\ f^* \zeta_x \\ f^* \zeta_y \end{bmatrix} + \left(\sigma \begin{bmatrix} 0 & \zeta_x & \zeta_y \\ \zeta_x & f^* \zeta_{xx} & f^* \zeta_{xy} \\ \zeta_y & f^* \zeta_{xy} & f^* \zeta_{yy} \end{bmatrix} - \begin{bmatrix} \frac{1}{4\pi s^2} & 0 & 0 \\ 0 & \frac{f^*}{8\pi s^4} & 0 \\ 0 & 0 & \frac{f^*}{8\pi s^4} \end{bmatrix} \right) \begin{bmatrix} f_{\text{ML}} - f^* \\ x_{\text{ML}} - x^* \\ y_{\text{ML}} - y^* \end{bmatrix} \quad (\text{G60})$$

with $\zeta = \sum_i Z_i p_i(x^*, y^*)$, $\zeta_\alpha = \sum_i Z_i \partial_\alpha p_i(x^*, y^*)$, and $\zeta_{\alpha\beta} = \sum_i Z_i \partial_{\alpha\beta} p_i(x^*, y^*)$. Solving this matrix equation for $x_{\text{ML}} - x^*$ and expanding to second order in σ yields:

$$x_{\text{ML}} - x^* = \frac{8\pi s^4 \sigma \zeta_x}{f^*} + \frac{32\pi^2 s^6 \sigma^2 (\zeta \zeta_x + 2s^2 [\zeta_x \zeta_{xx} + \zeta_y \zeta_{xy}])}{f^{*2}}. \quad (\text{G61})$$

The sums $\zeta, \zeta_\alpha, \zeta_{\alpha\beta}$ are random variables with mean zero just as Z_i are. It can be shown that the expectation value of $x_{\text{ML}} - x^*$ is zero (ie. the position is unbiased) by evaluating expectation values like

$$\langle \zeta \zeta_x \rangle = \left\langle \sum_{ij} Z_i p_i(x^*, y^*) Z_j \partial_x p_j(x^*, y^*) \right\rangle = \sum_i \langle Z_i^2 \rangle p_i(x^*, y^*) \partial_x p_i(x^*, y^*) \approx \iint p(x, y) \partial_x p(x, y) dx dy = 0 \quad (\text{G62})$$

with the second equality following from the independence of the Z_i and the third equality holding in the oversampled limit. Similarly,

$$\langle \zeta_x \zeta_{xx} \rangle = \langle \zeta_y \zeta_{xy} \rangle = 0 \quad (\text{G63})$$

Since $x_{\text{ML}} - x^*$ has an expectation value of zero, the variance in position can be found by squaring Equation G61 and taking the expectation value. To evaluate the variance in position, these expectation values are needed:

$$\langle \zeta^2 \rangle = \frac{1}{4\pi s^2} \quad (\text{G64})$$

$$\langle \zeta_x^2 \rangle = \langle \zeta_y^2 \rangle = \frac{1}{8\pi s^4} \quad (\text{G65})$$

$$\langle \zeta_{xx}^2 \rangle = \frac{3}{16\pi s^6} \quad (\text{G66})$$

$$\langle \zeta_{xy}^2 \rangle = \frac{1}{16\pi s^6} \quad (\text{G67})$$

$$\langle \zeta \zeta_{xx} \rangle = -\frac{1}{8\pi s^4} \quad (\text{G68})$$

$$\langle \zeta \zeta_x^2 \rangle = \langle \zeta \rangle \langle \zeta_x^2 \rangle = 0 \quad (\text{G69})$$

$$\langle \zeta_x^2 \zeta_{xx} \rangle = \langle \zeta_x^2 \rangle \langle \zeta_{xx} \rangle = 0 \quad (\text{G70})$$

$$\langle \zeta_x \zeta_y \zeta_{xy} \rangle = \langle \zeta_x \rangle \langle \zeta_y \rangle \langle \zeta_{xy} \rangle = 0 \quad (\text{G71})$$

$$\langle \zeta^2 \zeta_x^2 \rangle = \langle \zeta^2 \rangle \langle \zeta_x^2 \rangle \quad (\text{G72})$$

$$\langle \zeta \zeta_x^2 \zeta_{xx} \rangle = \langle \zeta \zeta_{xx} \rangle \langle \zeta_x^2 \rangle \quad (\text{G73})$$

$$\langle \zeta \zeta_x \zeta_y \zeta_{xy} \rangle = \langle \zeta \rangle \langle \zeta_x \rangle \langle \zeta_y \rangle \langle \zeta_{xy} \rangle = 0 \quad (\text{G74})$$

$$\langle \zeta_x^2 \zeta_{xx}^2 \rangle = \langle \zeta_x^2 \rangle \langle \zeta_{xx}^2 \rangle \quad (\text{G75})$$

$$\langle \zeta_x \zeta_y \zeta_{xx} \zeta_{xy} \rangle = \langle \zeta_x \rangle \langle \zeta_y \rangle \langle \zeta_{xx} \rangle \langle \zeta_{xy} \rangle = 0 \quad (\text{G76})$$

$$\langle \zeta_y^2 \zeta_{xy}^2 \rangle = \langle \zeta_y^2 \rangle \langle \zeta_{xy}^2 \rangle \quad (\text{G77})$$

which yield:

$$\langle (x_{\text{ML}} - x^*)^2 \rangle = \frac{8\pi s^4 \sigma^2}{f^{*2}} \left(1 + \frac{28\pi s^2 \sigma^2}{f^{*2}} \right) = \frac{2s^2 \tilde{\sigma}_f^2}{f^{*2}} \left(1 + \frac{7\tilde{\sigma}_f^2}{f^{*2}} \right) \quad (\text{G78})$$

Approximating the position errors as being distributed as a 2-D Gaussian with this variance and using Equation 69 gives:

$$\mathbb{E}[f_{j,\text{ML}}] = f_j^* \times \frac{2s^2}{2s^2 + \frac{2s_D^2 \tilde{\sigma}_{f_D}^2}{f_D^{*2}} \left(1 + \frac{7\tilde{\sigma}_{f_D}^2}{f_D^{*2}} \right)} \approx \boxed{f_j^* \left(1 - \frac{s_D^2 \tilde{\sigma}_{f_D}^2}{s^2 f_D^{*2}} - \left[\frac{7s_D^2}{s^2} - \frac{s_D^4}{s^4} \right] \frac{\tilde{\sigma}_{f_D}^4}{f_D^{*4}} \right)} \quad (\text{G79})$$